Multidimensional manipulation of wave fields based on artificial microstructures
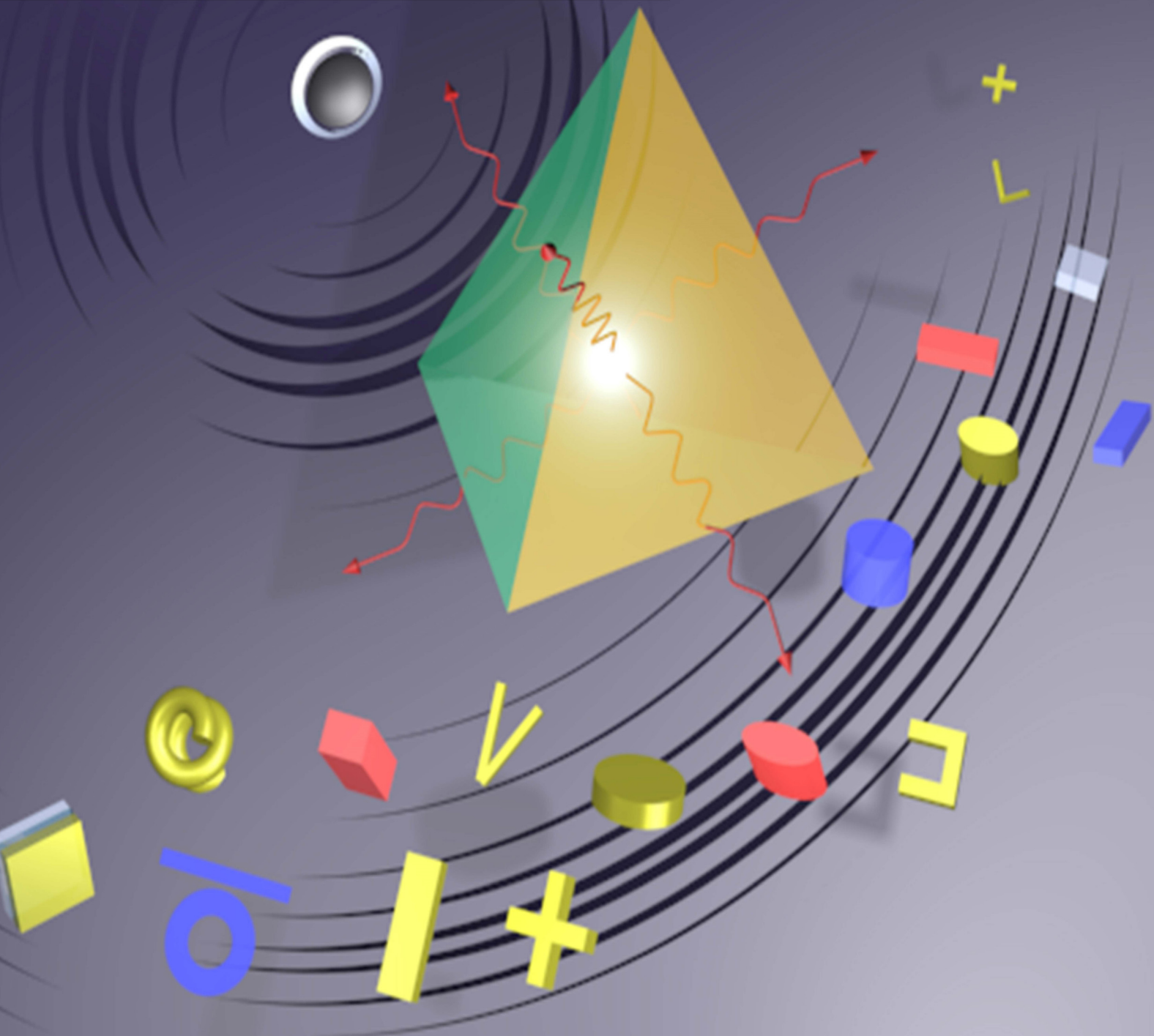
Yuebian Zhang, Hui Liu, Hua Cheng*, Jianguo Tian and Shuqi Chen*

Multidimensional manipulation of wave fields based on artificial microstructures

Yuebian Zhang[1], Hui Liu[1], Hua Cheng[1]*, Jianguo Tian[1] and Shuqi Chen[1,2,3,4]*

Artificial microstructures, which allow us to control and change the properties of wave fields through changing the geometrical parameters and the arrangements of microstructures, have attracted plenty of attentions in the past few decades. Some artificial microstructure based research areas, such as metamaterials, metasurfaces and phononic topological insulators, have seen numerous novel applications and phenomena. The manipulation of different dimensions (phase, amplitude, frequency or polarization) of wave fields, particularly, can be easily achieved at subwavelength scales by metasurfaces. In this review, we focus on the recent developments of wave field manipulations based on artificial microstructures and classify some important applications from the viewpoint of different dimensional manipulations of wave fields. The development tendency of wave field manipulation from single-dimension to multidimensions provides a useful guide for researchers to realize miniaturized and integrated optical and acoustic devices.

Keywords: metasurfaces; wave field manipulation; optics, acoustics; topological states

Introduction

To receive and send information, images and sounds are two primary information carriers for a person in his/her real life. The manipulation of electromagnetic (EM) and acoustic waves plays a fundamental role in the current information society. However, traditional components for wave field manipulations are often bulky and heavy, which limits the applications of these components in miniaturized and integrated devices. Artificial microstructures (also called meta-atoms) are some manmade subwavelength structures, which can resonate with EM, acoustic, or other kinds of waves. Metamaterials[1–3] and metasurfaces[4–9] that have three-dimensional (3D) and two-dimensional (2D) artificial microstructures respectively have been proposed to realize miniaturized and

integrated wave field manipulation devices in recent years. In addition, they can exhibit novel properties beyond natural materials and realize novel applications by carefully designing the geometrical parameters and the arrangements of artificial microstructures. Based on artificial microstructures, numerous applications, such as left handed metamaterials[10], metamaterial cloaks[11], zero-index metamaterials[12,13], hyperbolic metamaterials[14–16], photonic and phononic topological insulators[17–21], have been realized, demonstrating the powerful wave field manipulation abilities of the artificial microstructures.

Basically, different properties of wave fields can be viewed as different controllable dimensions that can be tailored by artificial microstructures. As shown in Fig. 1, for acoustic waves in the air, the primary manipulation dimensions are phase, frequency and amplitude. Because
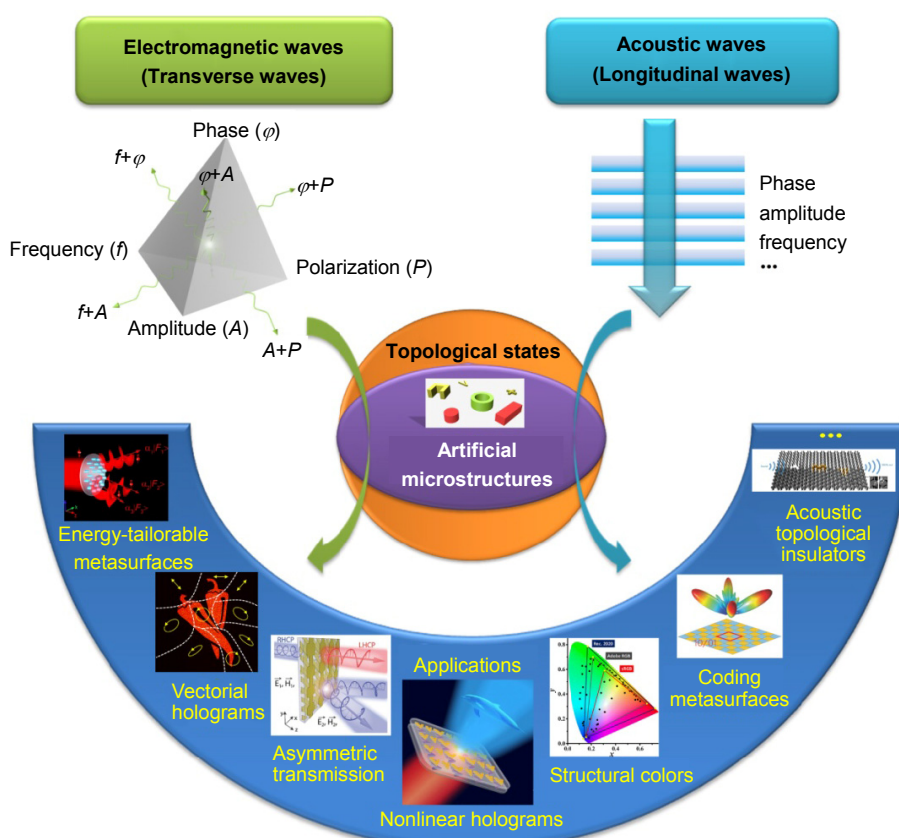
Fig. 1 | Overview of the multidimensional manipulation of wave fields based on artificial microstructures.

the airborne acoustic waves are longitudinal waves, they cannot exhibit different polarization states. However, for EM waves, the polarization state is also an important manipulation dimension due to the fact that the electric field vector is transversely polarized. Thus, the phase, polarization, amplitude and frequency constitute four basic dimensions of EM waves. On the other hand, with the help of artificial microstructures, the energy band structures of phonons and photons can also be manipulated. The arbitrary manipulation of these optical and acoustic dimensions is the core task of wave field manipulation. Over the past decades, researchers have done a lot of work on the one-dimensional manipulation of wave fields. Based on metamaterials and metasurfaces, the transmission, reflection, and absorption intensity of EM and acoustic waves can be easily manipulated. As a result, near perfect absorbers[22–24], Fano resonances[25], plasmonically induced transparency[26], antireflection metasurfaces[27,28], and some other amplitude manipulation applications have been proposed. By manipulating the polarization of EM waves, polarizers[29] and wave plates[30] have been realized. Based on the phase manipulation abilities of artificial microstructures, holograms[31],

beam deflectors[32–34], metalenses[35] and coding metasurfaces[36] have also been proposed in recent years. In addition, the frequency of EM waves can also be manipulated by nonlinear metasurfaces[37]. For more details about one-dimensional manipulation of wave fields, readers can refer to some previous review articles[1–9,31,32,35–41], which have reviewed the metamaterials and metasurfaces from different viewpoints. For example, Genevet et al. reviewed the development of metasurfaces from plasmonic to dielectric metasurfaces[6], Assouar et al. reviewed the design strategies of acoustic metasurfaces[9], Ding et al. reviewed the fundamentals and applications of gradient metasurfaces[32], Chen et al. mainly focused on the phase manipulation methods of metasurfaces[38], Glybovski et al. classified the metasurfaces based on their operational principles and functionalities[40], Sun et al. presented an overview on the working principles and applications of metasurfaces[41]. With the development of metamaterials and metasurfaces, the dimensions of wave field manipulation have extended from single-dimension to multidimensions[42–44], which have greatly expanded the scope of artificial microstructures. Therefore, a review about the multidimensional manipulations of wave fields

will provide a useful guide for researchers to design novel optical and acoustic devices.

In this paper, we focus on the recent developments of wave field multidimensional manipulations based on artificial microstructures. Firstly, we systemically discuss the 2D manipulation of EM waves, including the simultaneous manipulation of phase and amplitude, phase and polarization, amplitude and polarization, frequency and phase, and some other 2D manipulations of EM waves. Next, we briefly review the manipulation of acoustic waves from the viewpoint of different acoustic dimensions, including the amplitude, phase and energy band structure. Then, we review some important optical and acoustic applications in wave field manipulations based on artificial microstructures. In the last section, we provide a brief conclusion and an outlook of potential developments in this field.

Manipulation of wave fields

Manipulation of EM waves

Manipulating phase and amplitude of EM waves

Phase and amplitude constitute the complex amplitude of a wavefront, which carries the main information of an image. Arbitrary complex amplitude manipulation of EM waves plays a vital role in realizing high quality holograms[31,45,46] and optical illusions[47]. In addition, by tailoring the phase and amplitude of antennas simultaneously, numerous novel applications can be achieved, such as metasurfaces that can control the efficiencies of anomalous refraction[48–50], reflection[51,52], or diffraction beams[53–55]. To realize arbitrary complex amplitude manipulation of EM waves, different geometrical parameters of antennas should be designed subtly, and the phase and amplitude usually need to be controlled independently. Liu et al. proposed a metasurface with simultaneous phase and amplitude manipulation of linearly polarized (LP) light based on C-shaped antennas[53]. As shown in Fig. 2(a), the transmission amplitude of the antenna array can be controlled by changing the orientation angle θ of the C-shaped antennas. At the same time, the phases of the antennas can be manipulated by changing their arm lengths and the open angles (Fig. 2(b)). Hence, by tailoring all these geometrical parameters simultaneously, both the transmission amplitude and the phase of the converted LP light can be manipulated independently and simultaneously. Based on this method, broadband terahertz metasurface gratings that can control the amplitudes of anomalous diffraction orders have been proposed. However, the efficiencies of these metasurface gratings are limited below 25% due to the fundamental limits of ultrathin plasmonic metasurfaces[56]. For metasurfaces operate in reflective scheme, one method to improve the efficiency is to use the metal–insulator–metal (MIM) configuration[57]. Based on this configuration, Kim et al. proposed a metasurface that can control the amplitude and phase of the local reflection coefficient independently[51]. The amplitude can be changed from 0 to 0.6725 by rotating the nanorod, and the phase can cover the full 2π range by changing the length of the nanorod. This complex amplitude manipulation ability enables the design of optical Dolph-Tschebyscheff reflectarrays that can minimize the sidelobe levels of radiation patterns. To manipulate the complex amplitude of circularly polarized (CP) light, one can utilize the Pancharatnam–Berry (PB) phase by rotating the structure and control the amplitude by changing the size of the structure[58,59]. Li et al. proposed a metasurface that can generate Airy beams for CP incident light based on gold (Au) nanorods[58], as shown in Fig. 2(c). When CP light incidents on a nanorod with a rotation angle θ, part of the CP light will convert into its cross-polarized states and acquire a PB phase $\Phi = 2\sigma\theta$, where $\sigma = \pm 1$ represents the left-handed circularly polarized (LCP) and right-handed circularly polarized (RCP) light, respectively. Thus, by arranging the nanorods in orthogonal directions, 0 and π phase changes can be achieved. In addition, by choosing nanorods with different lengths, the amplitude of the cross-polarized light can be modulated to fit the normalized Airy function. Based on this method, Airy beams with both phase and amplitude modulation can be achieved. However, these manipulation schemes based on changing the structure size are usually difficult to achieve broadband operations due to the resonant properties of the structures. Recently, Lee et al. proposed a metasurface that can realize broadband complex amplitude holograms based on X-shaped structures[60]. The X-shaped structure can be viewed as a superposition of two nanorods with different orientation angles. If the excited modes can be modeled by two independent electric dipoles under CP light incidence, the transmission of the cross-polarized light can be simply changed by varying the intersection angles of the two nanorods, as shown in Fig. 2(d). In addition, the phase of the cross-polarized light can be changed by rotating whole X-shaped structure. That is to say, both the phase and amplitude can be manipulated by choosing different
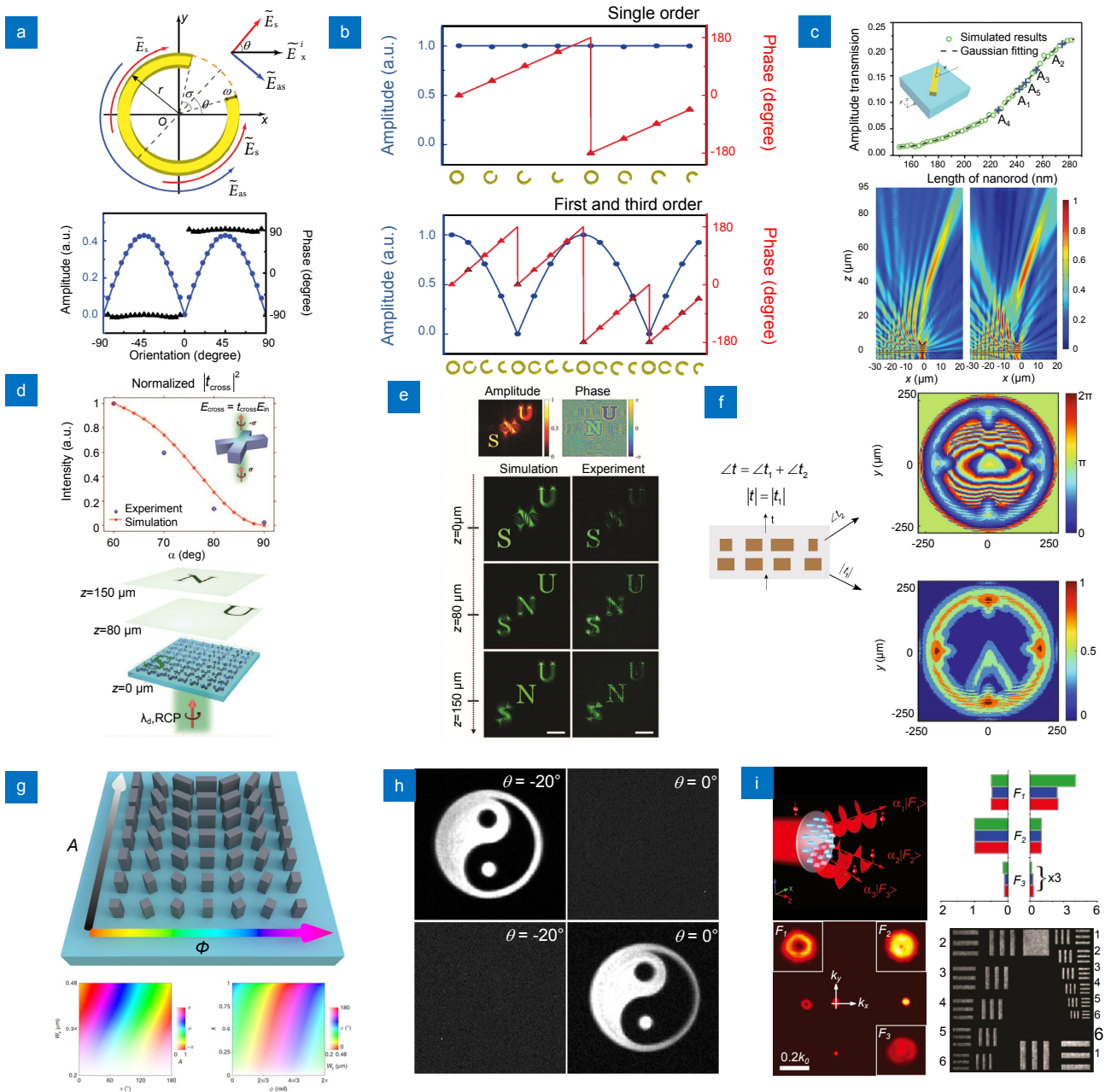
Fig. 2 | (**a**) Schematic of the C-shaped antenna used to control the phase and amplitude of linearly polarized light simultaneously (upper panel) and simulated transmission amplitude and phase of an antenna array for different orientation angle θ (lower panel). (**b**) Simulated amplitude and phase of the transmitted y-polarized light for different antennas with different orientation angle θ and geometrical parameters under x-polarized normal incidence. (**c**) Upper panel: simulated amplitude of the converted CP light for different nanorods with different lengths. Inset shows the schematic of the gold nanorod. Lower panels: simulated electric field distributions of the Airy beams with simplified amplitude modulation (left) and without amplitude modulation (right). (**d**) Simulated and measured cross-polarized transmission for X-shaped structures with different intersection angles (upper panel) and schematic of the designed hologram (lower panel). (**e**) Upper panels: amplitude and phase profiles of the designed hologram. Lower panels: simulated and measured holographic images at proper image planes. (**f**) Left panel: schematic of the bilayer metasurface that can generate complex amplitude holograms. Right panels: phase (upper) and amplitude (lower) profiles of the designed hologram. (**g**) Upper panel: schematic of the structures used to independently and completely control the transmitted phase and amplitude. Lower panels: simulated phase and amplitude for structures with different lengths and rotation angles. (**h**) Measured holographic images at different observation angles. The upper two images correspond to the metasurface with a phase gradient. The lower two images correspond to the metasurface with same intensity distributions as the upper metasurface but without phase gradient. (**i**) Left panels: schematic of the energy tailorable multifunctional metasurface (upper) and measured light distributions of three vortex beams with order of 3, 1, 0, respectively (lower). Right panels: the designed (red), calculated (blue) and measured (green) energies of each functionality for different samples (upper) and measured image of 1951 USAF resolution test target realized by a metasurface (lower). Figure reproduced from: (a–b) ref.[53], Wiley-VCH; (c) ref.[58], Wiley-VCH; (d–e) ref.[60], Royal Society of Chemistry; (f) ref.[61], Nature Publishing Group; (g–h) ref.[62], Nature Publishing Group; (i) ref.[63], Wiley-VCH.

combinations of the two orientation angles according to an expanded PB phase theory. As a result, this type of structure is resistant to fabrication errors and can realize broadband operation. As an example, broadband complex amplitude holograms that can reconstruct three letters on different image planes have been demonstrated, as shown in Fig. 2(d,e). Besides the methods mentioned above, the phase and amplitude can also be manipulated simultaneously by using few-layer metasurfaces[61]. As shown in Fig. 2(f), the metasurface contains two layers: the nanodisks in the bottom layer are used for manipulating the amplitude of the transmitted light and the nanoposts in the top layer are used for manipulating the phase. The total phase of the transmitted light is the summation of the phases contributed by the two layers. Both the phase and the amplitude are manipulated by changing the radius of these dielectric structures. Based on this method, 3D complex amplitude hologram that can display a clock evolving along the propagation direction has been achieved. Few-layer metasurfaces provide more degrees of freedom to manipulate the complex amplitude of EM waves and can realize polarization-insensitive operation, which provide a promising way to realize more novel functions based on the full control of phase and amplitude.

In the past few years, one difficulty in manipulating the complex amplitude of EM waves is realizing complete control of amplitude from 0 to 1. Recently, several works based on few-layer metasurfaces and/or dielectric metasurfaces have partially solved this problem[61–64]. Overvig et al. proposed a metasurface that can completely tailor the amplitude and phase at near-infrared (NIR) wavelengths by using amorphous silicon (a-Si) structures[62]. As shown in Fig. 2(g), the amplitude of the converted CP light can be continuously changed from 0 to 1 by varying the lengths of the nanostructures, and the phase can be continuously changed from 0 to 2π by varying the orientation angles of the nanostructures. Artifact-free holographic images and holograms with separately encoded amplitude and phase profiles have been demonstrated based on this metasurface platform. As shown in Fig. 2(h), two metasurfaces with identical intensity profiles but distinct phase gradient can reconstruct holographic images at different observation angles. Taking advantage of complete and simultaneous manipulation of phase and amplitude, energy tailorable multifunctional metasurfaces have been proposed[63]. As shown in Fig. 2(h), spin-selective metasurfaces that can generate

three vortex beams with different topological charges and controllable energy ratios have be experimentally realized based on a-Si elliptical nanopillars. In addition, direct imaging of a calibration test target with low noises have also been realized. In principle, the functionalities can be arbitrarily designed as long as the interferences in k-space between different channels are weak enough. Based on these modulation methods and design strategies, numerous novel functions related to energy control and complex amplitude manipulation are foreseen in the future.

Manipulating phase and polarization of EM waves

Plane EM waves in free space are transverse waves, which leads to many unique and intriguing phenomena compared with longitudinal waves, such as birefringence, optical activity and vector light fields. Metasurfaces are suitable platforms to manipulate the polarization states of EM waves at sub-wavelength scale. In the past few years, many polarization manipulators, such as polarization convertors[65–70] and optically active devices[71,72], have been proposed based on metasurfaces. However, most of these works are designed to realize a single functionality, which cannot fulfill the demand of modern optics for multifunctional devices. By manipulating the phase and polarization of EM waves simultaneously, the functionalities of a single metasurface can be greatly expanded, and novel functions, such as vector Bessel beams[73], vector vortex beams[74] and focused vector beams with sub-diffraction focusing spots[75], can also be achieved. In this section, we mainly focus on the discussion of three types of work related to simultaneous manipulation of phase and polarization: 1) polarization manipulators based on phase modulation; 2) complete control of phase and polarization distribution; 3) polarization dependent multifunctional phase gradient metasurfaces.

Arbitrary polarization states can be generated by superimposing two orthogonal polarization states with proper amplitude ratio and phase difference. If we use two subunits to produce two orthogonal polarization states and control the phase difference between them, and then place them together in a sub-wavelength distance, we can generate arbitrary polarization states in principle[76–82]. For example, Wu et al. proposed a reflective polarization generator that can produce arbitrary polarizations for LP incident light based on MIM structures[79]. As shown in Fig. 3(a), by arranging the Aluminum (Al) nanorods in an array with a constant orientation angle

gradient, LP incident light can be converted into two CP light with opposite handedness propagating in two different directions due to the PB phase. To generate LP light, two subunits with opposite phase gradients were combined. The offset between the two subunits introduced the desired phase difference between the co-propagating LCP and RCP light. The superposition of them in far-field generated the desired LP light. As shown in Fig. 3(b), different supercell designs with different position offsets and phase gradients can produce six different polarization states reflected to different directions. Compared with simple polarization convertors that only use periodic scattering anisotropic nanostructures, this method can separate the converted light from the background optical field due to the phase gradient of the metasurface. Besides the generation and manipulation of different polarization beams with uniform polarization distribution, realizing arbitrary polarization and phase distribution is also valuable for modern optics. Li et al. proposed a plasmonic metasurface that can control the polarization and phase distributions of light simultaneously based on the bilayer rectangular nano-aperture structures[83]. As shown in Fig. 3(c), the Au nano-aperture pairs can support waveguide modes between layers. As a result, the phase of the transmission light can be changed by changing the geometrical parameters and the relative positions of the nano-apertures. In addition, the polarizations of the transmission light are perpendicular to the major axis of the nano-apertures. By rotating the rectangular nano-apertures, the polarizations can be changed and an extra Berry phase term of $e^{i\theta}$ can be added to the transmitted light for CP light incidence, where θ is the rotation angle. As a result, full control of polarization and phase can be achieved. A radially polarized vector beam without a helical phase profile were then experimentally demonstrated based on this configuration. This method can also be used to realize vector beams with arbitrary phase distributions[84]. However, the efficiencies of these works are not very high due to the Ohmic losses of plasmonic structures. This problem can be solved by using dielectric structures[85] or few-layer metasurfaces[73,86]. Based on high-contrast a-Si elliptical nanoposts, Arbabi et al. realized several high efficiency metasurfaces that can completely control the phase and polarization for LP incident light at NIR wavelengths[85]. The phase and polarization can be tailored by changing the geometrical parameters and the rotation angles of the elliptical nanoposts, respectively. As shown in Fig. 3(d), one of the metasurfaces can generate and focus the radially and azimuthally polarized light for different LP incident beams. Another metasurface that can convert LP incident Gaussian beams into radially and azimuthally polarized Bessel–Gauss beams was also demonstrated, with measured transmission efficiencies reaching 96% and 97% for the x and y polarized incident beams, respectively. Recently, Deng et al. proposed a new method to realize arbitrary polarization and phase distributions by using "diatomic metasurfaces"[87]. As shown in Fig. 3(e), the unit cell of the metasurface consists of two orthogonal metal nanorods. Different from the former works that use PB phase or resonance phase, this work is based on the displacement-targeted phase[88], which can be continuously tuned by changing the global displacement of the metamolecule. The fundamental mechanisms of the polarization manipulation are similar to the polarization generators discussed above. The two orthogonal nanorods can produce two orthogonal LP beams with controllable amplitude ratio and phase difference, which can be tailored by changing the orientation angle of the metamolecule and the local displacement between the two nanorods, respectively. This method can realize phase manipulation robust against both wavelengths and incident angles, and can generate arbitrarily polarized light, including CP and elliptically polarized light. As a result, vectorial holograms with arbitrarily spatially varying polarizations can be achieved.

Polarization is an important degree of freedom to record optical information. By encoding different phase information or functions into different polarization channels, numerous polarization dependent multifunctional phase gradient metasurfaces can be realized[89–97]. The key to realizing these devices is to achieve polarization dependent phase responses, which are usually implemented by anisotropic nanostructures for LP light[98,99]. However, for CP incident light with opposite handedness, these nanostructures can only implement equal and opposite phase profiles if only PB phases are used[89,92]. Recently, Mueller et al. proposed a method that can implement two independent and arbitrary phase profiles on any pairs of orthogonal polarization states by combining both propagation phase and PB phase[95]. As shown in Fig. 3(f), by varying the dimensions and orientation angles of dielectric nanostructures that act as linearly birefringent wave plates, arbitrary and independent phase profiles can be achieved for two orthogonal polarization states. As a proof, a hologram metasurface that can produce a
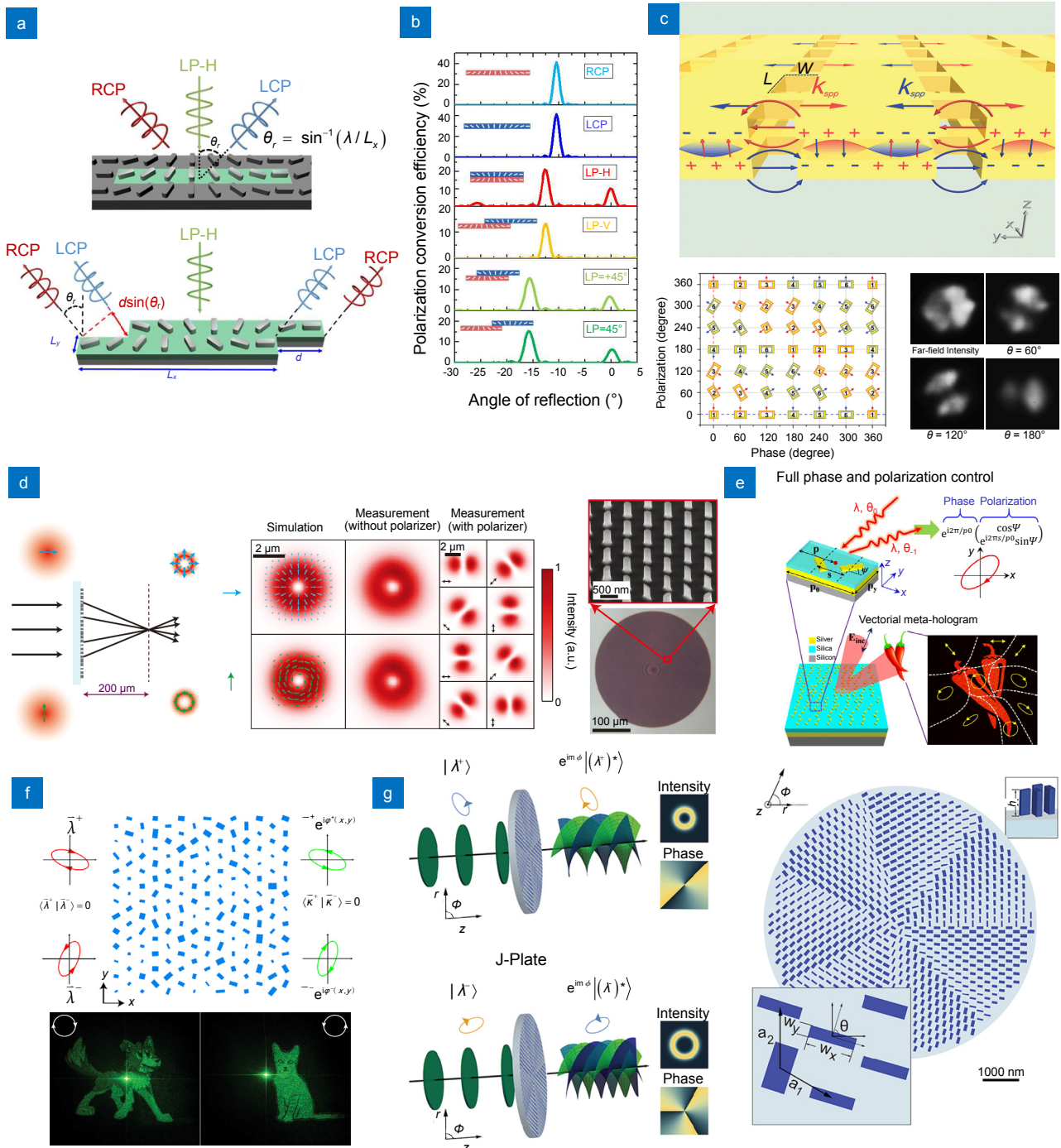
Fig. 3 | (**a**) Schematic of the reflective polarization generators based on phase gradient metasurfaces. (**b**) The simulated polarization conversion efficiency for each polarization. (**c**) Left: schematic of the bilayer nano-aperture structure used to control the polarization and phase simultaneously. Middle: schematics of the polarization and phase realized by nano-aperture pairs with various dimensions and orientations. Right: measured far-field intensity distributions of the generated radially polarized beam without and with a linear polarizer (oriented at angle θ) intercepted before the camera. (**d**) Left: schematic of the metasurface that can generate and focus the radially and azimuthally polarized light for different LP incident beams. Middle: simulated and measured intensity distributions of the vector beams. Right: optical (bottom) and scanning electron (top) microscope images of the metasurface. (**e**) Schematic of the diatomic metasurface for vectorial holography. (**f**) Upper panels: schematic of the metasurface that can implement two independent and arbitrary phase profiles on any pair of orthogonal polarization states by combining both propagation phase and PB phase. Lower panels: measured images of the chiral holograms for different CP incident light. (g) Schematic of the arbitrary SOC (left) and the typical J-plate design (right). Figure reproduced from: (a–b) ref.[79], American Chemical Society; (c) ref.[83], Wiley-VCH; (d) ref.[85], Nature Publishing Group; (e) ref.[87], American Chemical Society; (f) ref.[95], American Physical Society; (g) ref.[100], American Association for the Advancement of Science.

dog image for RCP incident light and a cat image for LCP incident light was experimentally realized. This strategy can not only realize polarization switchable multifunctional metasurfaces for arbitrary orthogonal LP and CP light, but also work for arbitrary orthogonal elliptical polarization light, which significantly expanding the scope of polarization dependent metasurfaces. Based on this strategy, arbitrary spin-orbital angular momentum conversion (SOC) have also been realized[100,101]. CP states of light correspond to the spin states of photons, which are related to the spin angular momentum (SAM) of light. Optical vortex beams are EM waves with a helical phase front $\varphi = l\theta$, where θ is the azimuthal angle in the transverse plane, l is the topological charge and related to the orbital angular momentum (OAM) of light[102–105]. Based on geometric metasurfaces with proper phase profiles, RCP (LCP) incident plane beams can be converted into LCP (RCP) output vortex beams with opposite topological charges[106–108]. However, this fundamental connection between the SAM and OAM limits the generation of arbitrary OAM states. By combining both propagation phase and PB phase, Devlin et al. decoupled the coupling between SAM and OAM, and realized arbitrary SOC for both CP light and elliptically polarized light[100]. As shown in Fig. 3(g), the metasurfaces consist of dielectric nanostructures with different dimensions and orientation angles. The output OAM states can be independently designed for arbitrary input orthogonal spin states. Recently, a novel method that can realize broadband SOC was proposed based on the diatomic metasurfaces[109]. This method utilized the PB phase and detour phase, which is similar to the strategy used in ref.[87]. The metasurface can independently generate different OAM states for RCP and LCP incident light in a wide range of incident angles. The coupling and decoupling between polarizations and phases produce abundant interesting phenomena. Novel physics and applications are waiting to be explored by arbitrarily and simultaneously manipulating the polarizations and phases.

Manipulating amplitude and polarization of EM waves
The reflection, transmission and absorption properties of periodic scattering anisotropic nanostructures are usually related to the polarization conversion of incident light. Deeply understanding the relationships between amplitude manipulation and polarization manipulation is vital to the realization of many useful optical devices, such as asymmetric transmission devices[110–117], chiral

metasurfaces[118–124] and polarization enabled image display[125,126]. Asymmetric transmission is a phenomenon that the total transmission of the forward and backward propagating light are different, which is closely related to the symmetry of the structure and the polarization conversion of the light[127]. If we use a complex Jones matrix (T-matrix) to describe the transmission of coherent light through a linear and reciprocal metasurface and write the T-matrix for the forward propagating light as:

$$T^{\mathrm{f}} = \begin{bmatrix} A & B \\ C & D \end{bmatrix}, \qquad (1)$$

where A, B, C and D are complex numbers. According to the reciprocity theorem, the T-matrix for the light propagating along the backward direction is

$$T^{\mathrm{b}} = \begin{bmatrix} A & -C \\ -B & D \end{bmatrix}. \qquad (2)$$

From the equations above we can know that the difference between the off-diagonal elements of the T-matrix determines the asymmetric transmission, which can be obtained from the polarization conversion efficiencies of the light for a given base vector. The asymmetric transmission occurs when $|B| \neq |C|$ and can be defined as $\Delta = |C|^2 - |B|^2$, which is affected by the symmetry of the metaatoms. To realize asymmetric transmission of LP light, the mirror symmetries with respect to a plane perpendicular to the propagation direction need to be broken, which is usually implemented by using few-layer metasurfaces[110–113,128–130]. For example, Huang et al. proposed a metasurface that can realize asymmetric transmission of LP waves based on few-layer twisted split ring resonators[111]. Two metallic split ring resonators were twisted 90° to each other and separated by a dielectric slab. Due to this special symmetry, strong asymmetric transmission only for LP waves was experimentally achieved at microwave frequency. To realize asymmetric transmission of CP light, Pfeiffer et al. proposed a bianisotropic metasurface composed of three patterned gold sheets[114], as shown in Fig. 4(a). By finely designing the sheet admittances of each layer, the metasurface can convert RCP incident light into LCP transmitted light for one incident direction and reflect RCP light for the opposite incident direction. The interference between these cascaded sheets can enhance the transmission of the converted CP light and the reflection of the undesired polarizations. As a result, the measured maximum transmission of the metasurface can reach 50% and the extinction ratio can reach 20:1 at NIR wavelengths

(shown in Fig. 4(b,c)).

Chirality is a universal geometrical property that refers to an object lacking any mirror-image symmetry. Compared with natural chiral objects, artificial chiral microstructures can have stronger optical chiral responses, which have attracted plenty of attentions from researchers due to their important roles in fundamental research and practical applications[131–134]. The optical chiral responses mainly arise from the different responses of chiral structures for LCP and RCP light, which can be roughly divided into two major phenomena: One is related to the different amplitude responses of CP light, including circular dichroism (CD)[135–140] and circular

conversion dichroism (CCD)[141–143]; the other is related to the polarization rotation of LP light due to the different refractive indexes for different CP light, termed optical rotation (OR) or optical activity or circular birefringence[144,145]. CD is a phenomenon that usually refers to the different absorption responses for different CP light, which is related to the OR through Kramers-Kronig relations. As a result, a chiral metasurface can always realize CD and OR effects simultaneously[146–148]. To realize chiral metasurfaces, the mirror-image symmetry of the unit cells should be broken, which can be implemented by using few-layer metasurfaces or 3D chiral structures. Based on dual-layer twisted-arcs, a CD of ~0.35 and a
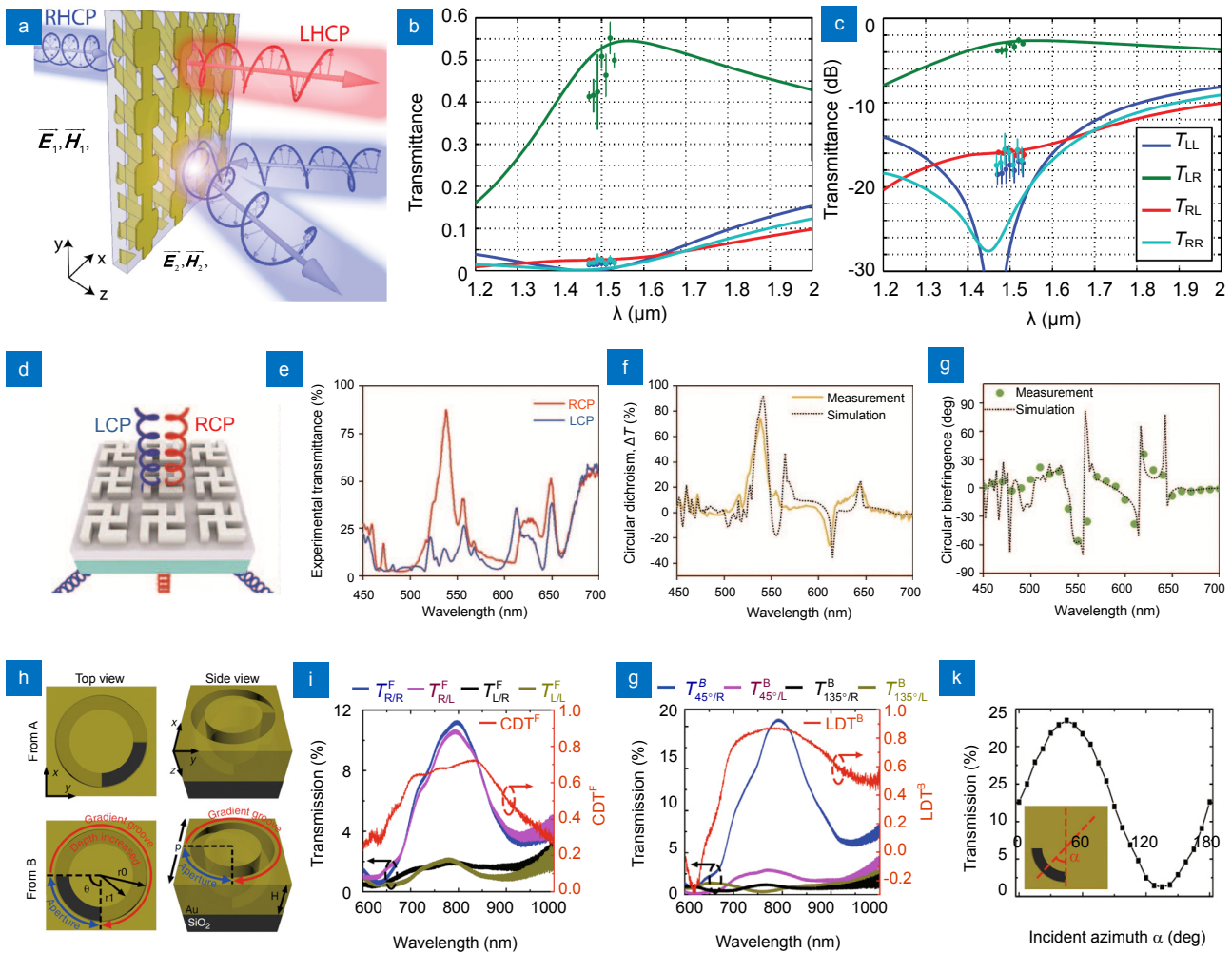

Fig. 4 | (a) Schematic of the metasurface that enables asymmetric transmission of CP light. Simulated (solid lines) and measured (circles) Jones matrix of the metasurface on linear **(b)** and logarithmic **(c)** scales. **(d)** Schematic of the optical response of the planar chiral metasurface. Measured zeroth-order transmission spectra **(e)**, CD spectra **(f)** and circular birefringence spectra (g) of the planar chiral metasurface. **(h)** Schematic of the 3D Janus helical structures in two enantiomeric forms. **(i)** Measured transmission spectra and CDTF spectrum of the metasurface in form A for different CP incident light in the forward direction. **(j)** Measured transmission spectra and LDTB spectrum of the metasurface in form A for different LP incident light in the backward direction. **(k)** Measured transmission spectrum for different azimuthal angles of the LP incident light. Figure reproduced from: (a–c) ref.[114], American Physical Society; (d–g) ref.[148], Nature Publishing Group; (h–k) ref.[154], Nature Publishing Group.

maximum polarization rotation of ~305°/λ have been experimentally achieved at NIR wavelengths[146]. In addition, the transmission at the polarization rotation peaks can be higher than 50%. It should be noticed that, due to the existence of linear birefringence, the OR power is dependent on the orientation of the incident LP light. One way to realize CD and OR without linear birefringence is to use structures with rotational disorder[147]. For example, for the metasurface consisting of two layers of asymmetric gold nanorods with fixed intersection angle, by randomly rotating the nanoantenna dimers around the z-axis, a globally isotropic response is achieved and pure chirality without linear birefringence can be realized. Besides the few-layer metasurfaces and 3D chiral structures, chiral metasurfaces can also be realized by using planar single-layer metasurfaces[121,148,149]. Recently, Zhu et al. proposed a planar chiral metasurface that can realize giant intrinsic chirality in the visible region[148]. As shown in Fig. 4(d), the metasurface consists of titanium dioxide gammadion nanostructures with four-fold (C4) symmetry. As a result, there is no linear birefringence and circular polarization conversion. The period of the metasurface is smaller than the targeted free space wavelength and greater than the effective wavelength in the substrate. By tailoring the resonance modes of the nanostructures and exciting higher-order multipolar modes, the normally incident RCP light can be transmitted in the zeroth order and LCP light can be diffracted into the first order. Thus, strong intrinsic chirality can be observed in the zeroth order transmitted light. As shown in Fig. 4(e–g), ~87% of the RCP light was transmitted in the zeroth order, and a giant CD in transmission of ~80%, together with a peak polarization rotation of ~60°, were experimentally achieved. CCD is a phenomenon related to the different circular polarization conversion efficiencies for LCP and RCP incident light, which is always connected with the asymmetric transmission of CP light[114,150–152]. It should be noticed that, for metasurfaces that preserve mirror symmetry in light propagation direction, strong CCD can still be realized if the nanostructures are chiral in the plane perpendicular to the light propagation direction[143,151].

Recently, a new kind of metasurface that can simultaneously realize optical chiral response and direction-controlled polarization conversion has been proposed[153,154]. As shown in Fig. 4(h), a metasurface composed of 3D plasmonic helical nanoapertures with gradient grooves was fabricated by means of one-step grayscale focused ion beam milling[154]. For CP incident light propagating in the forward direction, the metasurface can convert RCP incident light into LP transmitted light but block LCP incident light, as shown in Fig. 4(i). This phenomenon is different from the CD and CCD effects discussed above, because the circular dichroism in transmission (CDT) is mainly attributed to the different reflection responses for different CP light rather than the absorption or the circular polarization conversion. In the backward direction, the metasurface acts as a combination of a linear polarizer and a circular polarizer. Both the LCP and the RCP incident light will be converted into RCP transmitted light with similar intensities. As a result, no CDT occurs in the backward direction. However, linear dichroism in transmission (LDT) is realized in the backward direction. As shown in Fig. 4(j), only the LP incident light with component perpendicular to the aperture can be transmitted and converted into RCP light. In addition, the transmission intensity can be changed by varying the azimuthal angle of the LP incident light according to the Malus's law, as shown in Fig. 4(k). Thus, this metasurface can encode binary image for the forward CP incident light and encode grayscale image for the backward LP incident light simultaneously. These polarization dependent spectrum manipulation metasurfaces discussed above reveal the complex relationships between amplitude manipulation and polarization manipulation. How to realize broadband and high efficiency asymmetric transmission devices and chiral applications, such as circular polarizers[155] and chiral molecular detection devices[156], with structures easier to fabricate still has a long way to go. Another research direction in this field is realizing arbitrary amplitude manipulation for arbitrary pairs of orthogonal polarized light, which can greatly expand the optical information storage capacities of a single metasurface.

Manipulating frequency and phase of EM waves
To meet the growing demand for novel optical devices and multifunctional metasurfaces, phase gradient metasurfaces that can simultaneously work in different frequency bands need to be explored. Over the past few years, numerous multiwavelength metasurfaces, such as colorful metaholograms[157–161], multiwavelength achromatic metalenses[162–169] and super dispersive devices[170,171], have been proposed. On the other hand, the research interests in phase gradient metasurfaces have been extended from linear optical response to nonlinear optical

response[172–177]. When an incident fundamental beam with CP state σ incidents on a subwavelength nanostructure with an orientation angle of θ embedded in an isotropic nonlinear medium, the nth harmonic nonlinear polarizabilities for the CP state σ and -σ can be expressed as $\alpha_{\theta,\sigma,\sigma}^{n\omega} \propto e^{(n-1)i\theta\sigma}$ and $\alpha_{\theta,-\sigma,\sigma}^{n\omega} \propto e^{(n+1)i\theta\sigma}$, respectively, where ω is the angular frequency of the fundamental beam[172]. As a result, the generated nonlinear signals with polarization same as or opposite to the polarization of the incident fundamental beam will acquire a phase of $(n-1)\sigma\theta$ or $(n+1)\sigma\theta$, respectively. In addition, the processes of harmonic generation are related to the symmetries of the molecular configurations[172,177–179]. For CP incident light, a single nanostructure with m-fold rotational symmetry allows only harmonic orders of $n = (lm+1)$ for the same CP as the incident light, and $n = (lm-1)$ for the opposite CP light, where l is an integer. Thus, a nanostructure with three-fold rotational symmetry (C3) can generate second harmonic signal with opposite CP states, which has a phase of $3\sigma\theta$, but cannot generate third harmonic signals. However, a nanostructure with two-fold rotational symmetry (C2) can generate third harmonic signals with both the same and opposite CP states, which have phases of $2\sigma\theta$ and $4\sigma\theta$, respectively. In addition, for C4 nanostructures, only a third harmonic generation (THG) signal with opposite CP state to that of the incident light and a phase of $4\sigma\theta$ can be generated[172], as shown in Fig. 5(a). Based on the geometric phases and selection rules of nonlinear signals, nonlinear metasurfaces with continuously controllable phases can be realized. By coating a nonlinear active medium (PFO) on top of two phase gratings composed of C2 (nanorod) and C4 (nanocross) structures, THG signals with different CP states can be generated. By varying the orientation angles of the nanostructures to impart the desired phase gradients on the metasurfaces, the diffraction of THG signals can be tailored at will. As shown in Fig. 5(b), for the C2/PFO metasurface, THG signals with both the same and opposite CP states to that of the incident light were generated and diffracted into the ±1 and ±2 diffraction orders. However, for the C4/PFO metasurface, only the THG signals with the opposite CP states were generated and diffracted into the ±1 diffraction orders, which confirms the existence of the geometric phases and selection rules of nonlinear signals. Based on the nonlinear geometric phase, nonlinear metalenses[180] and nonlinear diffraction[181] for second harmonic generation (SHG) signals have also been real-

ized. Besides manipulating the phases of harmonic signals, the phases of nonlinear four-wave mixing (FWM) signals can also be manipulated[175,182]. As shown in Fig. 5(c), by using rectangular nanocavities in thin gold films with different aspect ratios, an additional momentum along the phase gradient direction can be provided[175]. Similar to the generalized Snell's law in linear optical response, a generalized phase-matching condition for FWM can also be derived by considering the additional momentum provided by the nonlinear metasurface. Thus, nonlinear blazed gratings for the FWM emission can be realized and their diffraction angles can be controlled by manipulating the phase gradients (grating periodicities) of the metasurfaces (shown in Fig. 5(d)). Different from the geometric phase working for CP nonlinear signals and realized by rotating the nanostructures, this method is based on the resonance phase and works for LP nonlinear signals. This method can also be applied to manipulate the phase of THG signals[183]. As shown in Fig. 5(e), based on the V-shaped gold nanostructures with different arm lengths and intersection angles, full 2π phase manipulation for the THG signals can be achieved under LP light incidence. Few-layer nonlinear hologram metasurfaces that can generate holographic images at the blue wavelength when illuminated by an infrared laser were experimentally achieved.

The phase manipulation of nonlinear signals provides a new way to separate the nonlinear beams from fundamental beams and realize background free optical devices. In addition, nonlinear metasurfaces can increase the information capacity of a single metasurface through additional information channels at nonlinear frequencies[184–187]. As shown in Fig. 5(f, g), Ye et al. proposed a metasurface that can generate different holographic images for fundamental beam and SHG beams of different CP states[184]. According to the theory of PB phase and selection rules of nonlinear signals, for an incident fundamental beam with CP state σ, a split ring nanoantenna with an orientation angle of θ can generate SHG beams with both same and opposite CP states, which have phases of $\sigma\theta$ and $3\sigma\theta$, respectively. In addition, the transmitted fundamental beam with a cross-CP state can acquire a PB phase of $2\sigma\theta$. That is to say, the linear and nonlinear signals can have different PB phases for a same nanostructure. Thus, it is possible to encode three different phase profiles for the three transmitted beams. Based on this idea, three independent holographic images of the letters 'X', 'R' and 'L' were

generated under LCP incident light for the transmitted RCP fundamental light, RCP second harmonic wave and LCP second harmonic wave, respectively. This method can also be applied to generate nonlinear optical vortices. As shown in Fig. 5(h), Li et al. proposed a metasurface that can simultaneously generate three optical vortices with different topological charges for linear beam with converted CP state and SHG beams with two different CP states[186]. In addition, the three optical vortices can be focused at different focal planes by adding parabolic phase distributions into the metasurface. This metasurface can provide threefold optical information channels compared with linear PB phase metasurfaces.

At the present stage, one problem that hinders the practical application of nonlinear metasurface is the low nonlinear frequency conversion efficiency. To solve this problem, Nookala et al. introduced the quantum well structure into the nonlinear phase gradient metasurface[188]. As shown in Fig. 5(i), the metasurface consists of semiconductor multi-quantum-well (MQW) heterostructure split-ring resonators and operates in reflective scheme. Due to the coupling of EM modes in nanoresonators and quantum-engineered intersubband nonlinearities in MQW semiconductor heterostructures, the nonlinear responses can be strongly enhanced. By taking advantages of nonlinear PB phases, beam steering
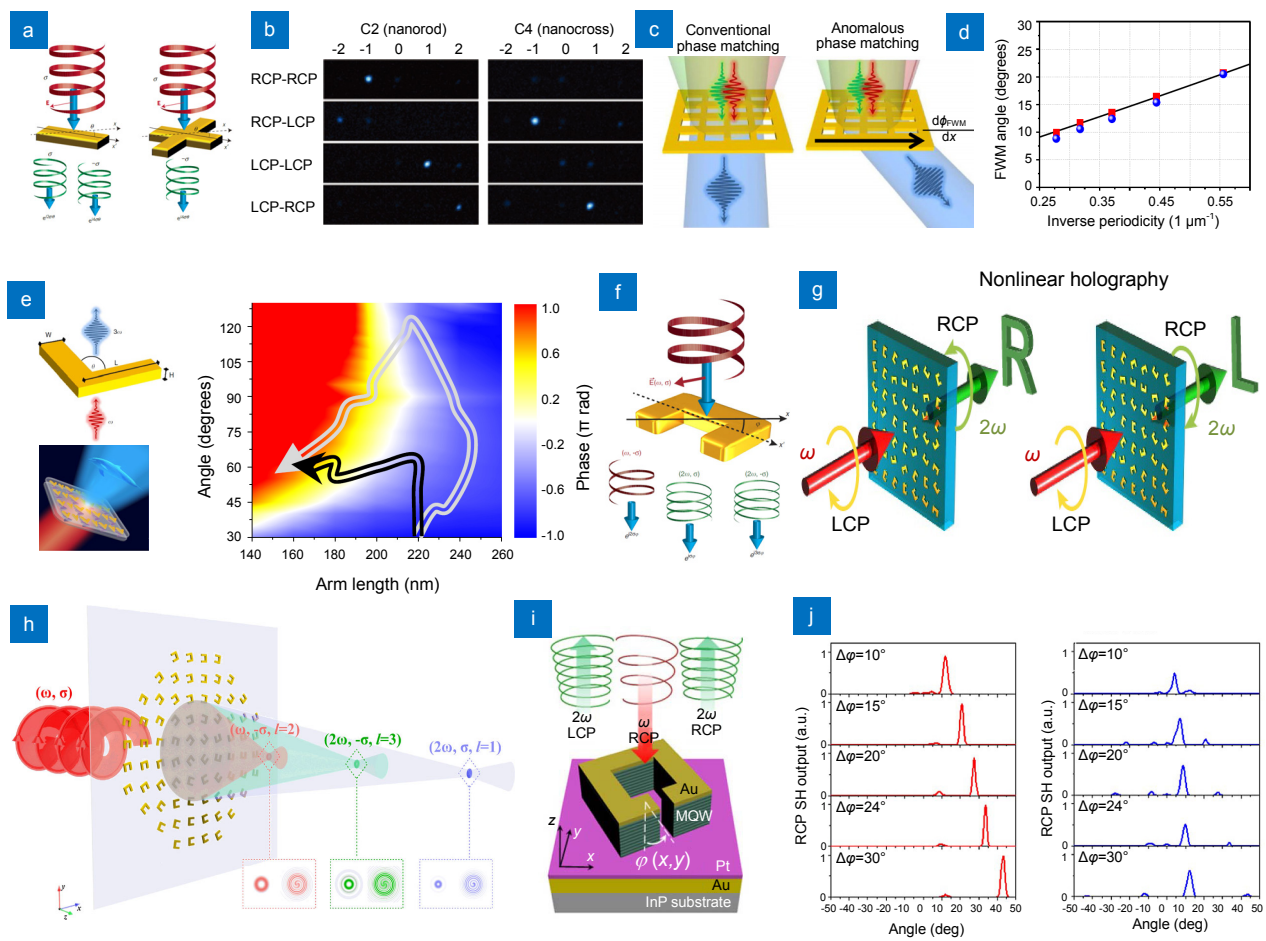

Fig. 5 | (**a**) Schematic of the THG signals and their phases for C2 and C4 nanostructures. (**b**) Measured THG signals from the C2/PFO and C4/PFO metasurfaces with a phase gradient of the nonlinearity. (**c**) Schematic of the anomalous phase matching condition for phase gradient metasurfaces. (**d**) Measured (blue circles), calculated (black line) and simulated (red squares) FWM emission angle as a function of the grating periodicity. (**e**) Left panels: schematic of the V-shaped gold antennas (upper) and the nonlinear hologram metasurfaces that work at THG wavelength (lower). Right panel: the phase of the THG signals for V-shaped antennas with different arm lengths and intersection angles. (**f**) Schematic of the linear and nonlinear PB phases for a split ring resonator. (**g**) Schematic of the nonlinear metasurface that can generate different SHG holographic images for different CP states. (**h**) Schematic of the nonlinear metasurface that can simultaneously generate three focused optical vortices with different topological charges and different focal lengths. (**i**) Schematic of the unit cell of the nonlinear phase gradient metasurface based on quantum well structure. (**j**) Far field profiles of RCP and LCP second harmonic wave output from the metasurfaces with different phase gradients. Figure reproduced from: (a–b) ref.[172], Nature Publishing Group; (c–d) ref.[175], Nature Publishing Group; (e) ref.[183], Nature Publishing Group; (f–g) ref.[184], Nature Publishing Group; (h) ref.[186], Wiley-VCH; (i–j) ref.[188], Optical Society of America.

of SHG signals with relatively high efficiency has been experimentally realized (shown in Fig. 5(j)). Besides the nonlinear optical responses, the rotational Doppler effect can also change the frequency of the incident light, which can be interpreted by the angular momentum transfer of light[189,190]. Based on the phase gradient metasurface, Georgi et al. have experimentally observed the rotational Doppler frequency shift induced by spin-orbit coupling of light[189]. When a CP light passes through the rotating metasurface, the cross CP reflected light will acquire a Doppler frequency shift, which is proportional to the rotational angular frequency of the metasurface and the total transferred angular momentum. The combination of frequency manipulation and phase manipulation greatly expands the scope of linear and nonlinear optics, which certainly will bring out numerous novel optical devices.

Other 2D manipulations of EM waves

Besides the 2D manipulation of EM waves discussed above, other multidimensional manipulations can also be realized based on the platform of metasurfaces. For example, by manipulating the frequency and amplitude of EM waves simultaneously, nonlinear harmonic generation enhancement metasurfaces for enhancing the SHG[191–195] and THG[196–198] signals have been realized. The frequency and polarization of EM waves can also be manipulated simultaneously by involving nonlinear materials[199,200]. In addition, the time evolution of EM waves can also be viewed as a controllable degree of freedom. All optical modulation of light polarization at picosecond timescales has been realized based on a nonlinear aniso-tropic metasurface[201]. By using gold cut-disk resonators that have strong coherent nonlinear responses, ultrafast optical modulation of SHG and THG signals can be realized on a subpicosecond timescale[202]. Recently, Keren-Zur et al. demonstrated that spatiotemporally tailored terahertz wavepackets can be generated by nonlinear metasurfaces[203]. These works demonstrate the extensive and powerful abilities of metasurfaces in EM wave manipulation. The simultaneous manipulation of two properties of EM waves will further expand the scope of metasurfaces and realize more advanced functions.

Manipulation of acoustic waves

Manipulating phase and amplitude of acoustic waves

Different from optical wave, sound waves are essentially mechanical waves. Sound waves travel through the fluid systems such as air and water only in a longitudinal wave pattern, while transverse wave mode can exists in solid elastomers. A sound field is described by amplitude and phase. As a 2D counterpart of acoustic metamaterials, acoustic metasurface are thought to be an effective way to control the acoustic field by modulating the amplitude and phase. The acoustic absorption metasurface can control the amplitude of acoustic absorption spectrum by designing resonance unit. The increase of energy density caused by the acoustic resonator can significantly increase the total energy dissipated by the material[204]. The acoustic absorption metasurface has the advantages of subwavelength size, small volume and good absorption capacity of low-frequency band, which are not provided by traditional acoustic absorption materials. According to the resonance unit structure, the sound absorption materials can be divided into membrane type[205,206], Helmholtz type[207,208] and Fabry-Pérot type[209,210]. By combining monopole resonance with dipole resonance, Yang et al. constructed a degenerate subwavelength membrane resonator and experimentally achieved a perfect absorption rate of 99.7% of the low frequency wave[206]. Based on Helmholtz resonators, a subwavelength resonant panel for low-frequency quasiperfect sound absorption was proposed which uses the accumulation of cavity resonances due to the slow sound phenomenon[208]. In Fig. 6(a), Yang et al. presented a folded Fabry-Pérot tube array for realizing structures with target-set absorption spectra and a sample thickness close to the minimum value decided by causality[210]. This method achieved the absorption spectrum close to the theoretical limit in the semi-infinite frequency range shown in Fig. 6(b). In addition, by constructing an additional phase distribution at the interface, acoustic metasurface can achieve arbitrary regulation of the wavefront phase. The acoustic structural units constitute the acoustic metasurface and each of them can independently modulate the phase of the acoustic wave in the range of 0-2π, forming a specific phase distribution on the emission surface of the metasurface[211]. For the concept of computer binary units that was introduced into the acoustic system[212], Xie et al. implemented coding acoustic metasurfaces by using two coding elements with equal amplitudes and a phase difference of π to represent '0' and '1' in the binary system, respectively[213]. Phases of acoustic waves transmitting through the coding elements of "0" and "1" are shown in Fig. 6(c). When two coding elements are arranged according to a specific coding sequence, the coding acoustic metasurfaces has the function of specific regulation of sound waves. In Fig. 6(d),
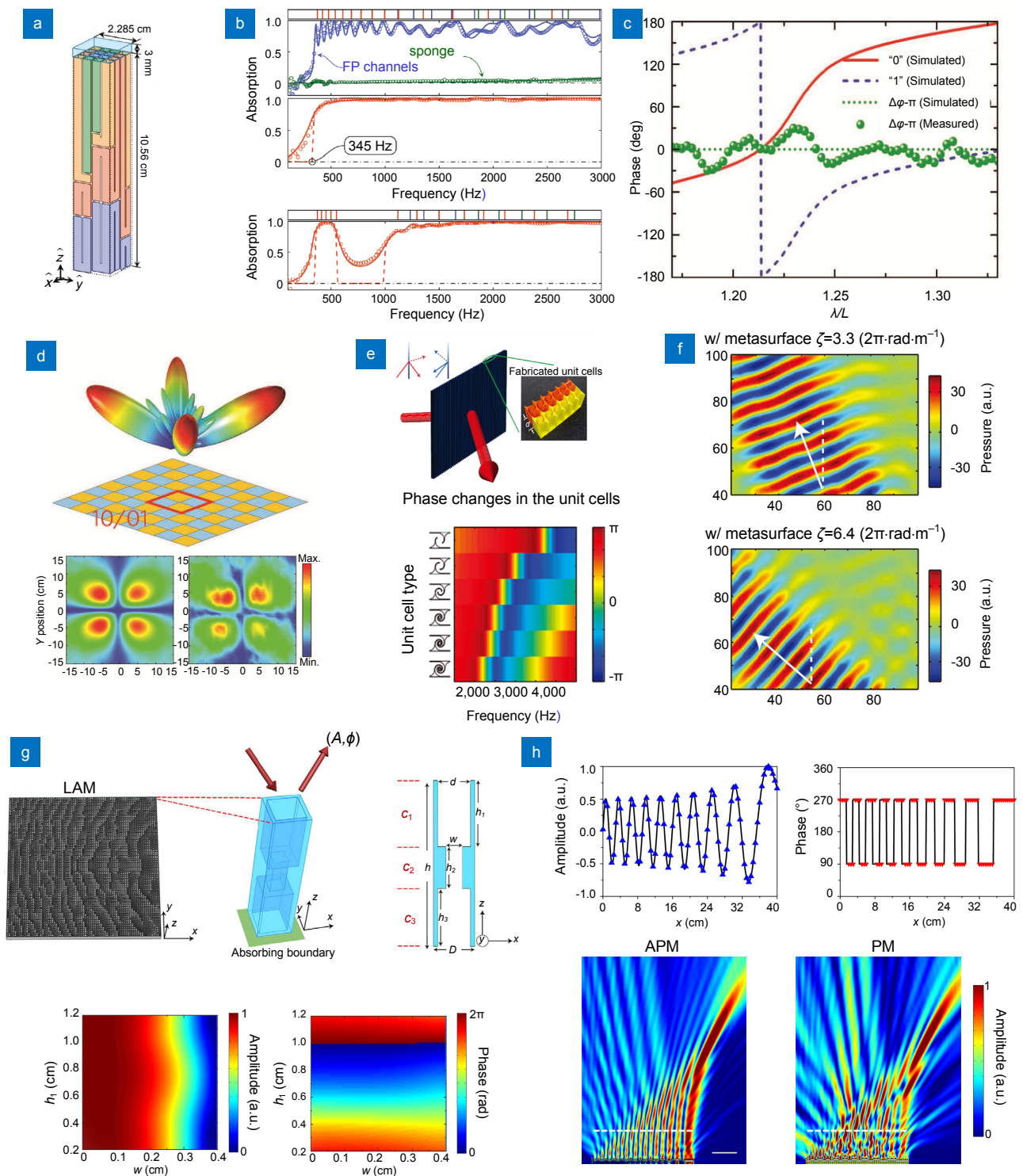
Fig. 6 | (**a**) Schematic of the folded Fabry-Pérot tube array for realizing structures with target-set absorption spectra. (**b**) Absorption spectra caused by Fabry-Pérot resonance, which is close to the theoretical limit in the semi-infinite frequency range. (**c**) The transmission phase of two coding elements. (**d**) Simulated far field distribution (upper) and simulated (lower left) and measured (lower right) field amplitude distributions of the transmitted waves divided into four beams when coding elements are distributed in a checkerboard pattern. (**e**) Schematic of generalized Snell's law realized by a series of tapered labyrinthine metamaterials (upper) and the phase changes of six types of unit cells (lower). (**f**) Measured anomalous refraction caused by controlling the wavefront phase with arrangement of the unit cells. (**g**) The decoupled effect of amplitude-phase (lower) caused by the holey structured lossy acoustic metamaterial (upper). (**h**) Upper panels: amplitude (left) and phase (right) profiles of the lossy acoustic metamaterial for generating the Airy beam. Lower panels: comparison of the Airy beam formed by amplitude phase modulation (APM) (left) and Phase modulation (PM) (right). Figure reproduced from: (a–b) ref.[210], Royal Society of Chemistry; (c–d) ref.[213], Wiley-VCH; (e–f) ref.[216], Nature Publishing Group; (g–h) ref.[226], Nature Publishing Group.

the reflected waves are divided into four beams with symmetrical azimuth distribution when the coding sequence is in a 2D checkerboard pattern. The beam-splitting effect enables acoustic coding metasurfaces to be used in acoustic antennas. Based on generalized Snell's law[214], Li et al. and Xie et al. designed reflective and transmissive acoustic metasurfaces, respectively, which realized arbitrary regulation of the acoustic wavefront[215–217]. Through arbitrary regulation of the wavefront phase of acoustic waves, some interesting phenomena such as anomalous reflection[218,219] and refraction[216,220,221], asymmetric propagation[222,223], acoustic vortex field[224] and directional control[213,225] were realized. Figure 6(e) shows the generalized Snell's law realized by a series of tapered labyrinthine metamaterials[216]. The phase changes of six types of unit cells are shown in Fig. 6(e), which can cover a complete 2π range. By controlling the phase of the wavefront, the metasurfaces can realize special acoustic effects which traditional acoustic devices cannot, such as anomalous refraction shown in Fig. 6(f), extraordinary beam-steering and negative refraction. Commonly, the structure units of metasurfaces are usually unable to adjust the amplitude and phase of acoustic waves independently at the same time and the unavoidable losses make it difficult to control coupling, which limits the ability of metasurfaces to control the acoustic field. Recently, a type of metasurfaces capable of achieving amplitude and phase modulation separately was proposed[226,227]. Zhu et al. studied the decoupling between the amplitude and phase of reflected acoustic waves by changing the structural parameters of the pipeline, as shown in Fig. 6(g)[226]. By deliberately introducing energy loss in a controlled manner, a holey lossy acoustic metamaterial was designed to arbitrarily adjust the amplitude and phase of acoustic wave. It is important to improve the accuracy and flexibility of sound field control. Figure 6(h) provides the comparison of the Airy beam formed by amplitude-phase modulation (APM) and phase modulation (PM), which obviously shows that APM Airy beam has a better quality than the one formed by PM. The APM of acoustic metasurface is flexible and adjustable and has a broad application prospect. Based on the decoupled modulation of phase and amplitude, a metasurface with coating unit cells and perforated panels was designed to achieve high-quality holograms[227].

Manipulating energy band structure of phonons
Phonon crystals, a periodic system of artificial scatterers,

provide periodic potential energy for acoustic waves. When acoustic wave travels through a phonon crystal, it has an energy band structure similar to the electronic system, which provides a possibility for the implementation of topology characteristics in phonon systems. To realize the topological phase transition of phonon crystal, time-reversal symmetry or spatial inversion symmetry should be broken. In acoustic systems, it is difficult to break the time-reversal symmetry, for phonons are low in energy and can hardly interact with magnetic fields, electrons and photons. In 2014, Alù et al. introduced a circulating fluid into a resonant ring cavity, and the acoustic Zeeman effect, making the degenerate counterpropagating azimuthal resonant modes split at the present of circulating fluid, was predicted[228]. Acting as acoustic magnetic field, fluid is introduced into the acoustic system. In 2015, acoustic topological Chern insulator was predicted by Yang et al. and Ni et al. by adding air flow to break time-reversal symmetry in the graphene lattice[229,230]. Figure 7(a) shows that the degeneracy of $K(K')$ points in the graphene lattice is opened by airflow and a complete band gap appears. For the breaking of time reversal symmetry, two bands at lowest energy carrying opposite nonzero Chern numbers and two edge states distributing on different surfaces propagate in opposite directions, as shown in Fig. 7(a)[230]. Due to the difficulty in controlling the air flow in the experiment, the acoustic Chern insulator was not observed until 2019[231]. For the system with time-reversal symmetry, acoustic quantum spin hall effect was realized. It is found that the pseudospin can be constructed by conjugate states, and the Kramers degeneracy can be replaced by the symmetry of the lattice in Bose system[232]. In 2016, He et al. used the symmetry of the lattice to construct the accidental degenerated double Dirac cone in phononic crystals, and the acoustic quantum spin Hall effect was observed experimentally for the first time[233]. The pseudospin is constructed by the hybridization of Bloch mode, and the band inversion between p-band and d-band is realized by the interaction of pseudospin-orbital coupling. Figure 7(b) shows two pairs of interface states with opposite propagation directions at the interface between topological trivial and topological nontrivial phononic crystals, which are robust and correspond to two conjugate states. In condensed matter, in addition to the intrinsic degrees of freedom such as spin and charge, solid materials also have valley degree of freedom, which exists at the singularity of the band

structure. Liu's group introduced valley degree of freedom into 2D acoustic phononic crystal, and a pair of topological protected interface states appear at the boundary between two phononic crystals with different valley phases[234,235]. As shown in Fig. 7(c), based on hexagonal lattice, the 2D phononic crystals consist of triangular scatterers[234]. When mirror symmetry is broken by rotating triangular scatterers, the Dirac cone in the $K(K')$ points is opened to form a band gap. A pair of ex-

treme points, appearing on the upper and lower band near $K(K')$ points, carry the opposite vortex on two unequal corners of the hexagonal lattice. Study finds that when the scatterers turn to opposite angle, the phononic crystal will be in different valley Hall phases, and two crystals in different valley Hall phases will produce a pair of valley chiral boundary transfer states shown in Fig. 7(c), whereas two crystals in the same valley Hall phase have none. In addition, the valley state is also extended to
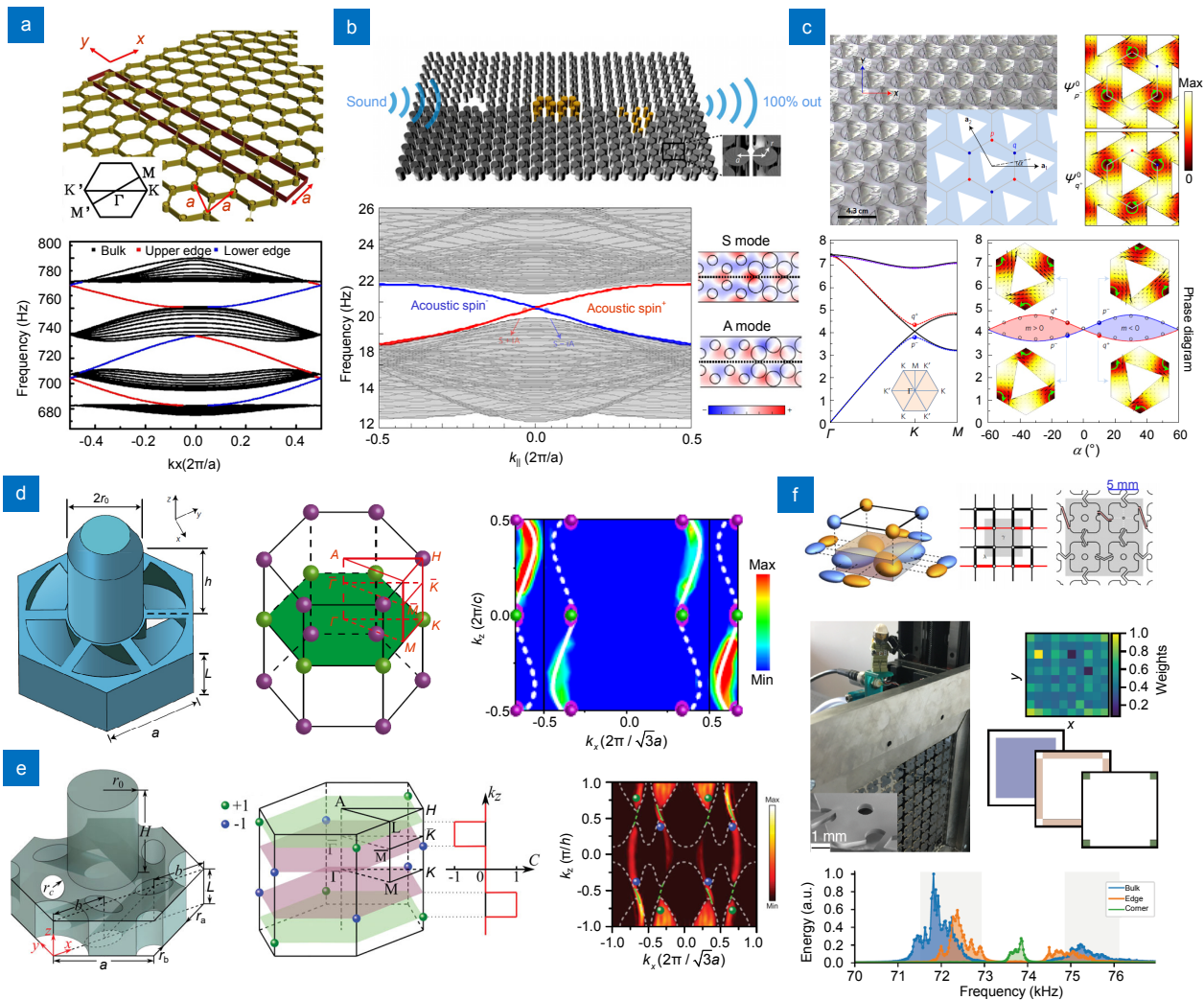

Fig. 7 | (**a**) Schematic of the topological Chern insulators (upper) and the projected band diagram of the sonic crystal (lower). The red and blue lines represent the edge states distributed on different edges. (**b**) Upper panel: schematic of the transmission of the acoustic quantum spin hall effect. Lower panel: calculated projected band diagram of the topological phononic crystal. The red and blue lines represent two pairs of interface states with opposite propagation directions distributed on different interfaces. (**c**) Upper panels: schematic of the two dimensional acoustic phononic crystal (left) and the valley states (right). Lower panels: the band diagram (left) and the band transition diagram (right). (**d**) Schematic of the phononic crystal of type-I Weyl points (left) and the distribution of type-I Weyl points in Brillouin zone (middle). Fourier transforms of the surface wave fields on the XZ plane that show the Fermi arc of type-I Weyl points(right). (**e**) Schematic of the phononic crystal of type- II Weyl points (left) and the distribution of type- II Weyl points in Brillouin zone (middle). Fourier transforms of the surface wave fields on the $XZ1$ plane that show the Fermi arc of type-II Weyl points (right). (**f**) Upper panels: schematic of the quantized quadrupole (left), the corresponding tight bound model (middle) and the corresponding structural unit (right). Middle panels: diagram of experimental equipment (left) and the corresponding distribution of the bulk, edge and corner response at an arbitrary frequency (72.0 kHz) (right). Lower panel: the frequency regions of bulk, edge and corner states. Figure reproduced from: (a) ref.[230], Institute of Physics; (b) ref.[233], Nature Publishing Group; (c) ref.[234], Nature Publishing Group; (d) ref.[238], Nature Publishing Group; (e) ref.[239], American Physical Society; (f) ref.[248], Nature Publishing Group.

the double-layer triangular scatterers, which shows more abundant topological phases[236].

Recently, in 3D phononic crystals, topological semimetals have drawn much attention. The typical representative of topological semimetals is Weyl semimetal, which carries two-fold degeneracy points in wavevector space, around which the quasi-particles resemble the massless Weyl fermions from the standard model. In Weyl semimetal, a pair of opposite chiral Weyl fermions carrying topological charge +1 or -1 connect with each other by a nontrivial surface state called the Fermi arc in the surface Brillouin zone. Based on graphene model, synthetic gauge flux was introduced in the 3D phononic crystal by engineering the coupling in the z direction. Two types of Weyl point models were proposed by Meng et al.[237], and observed experimentally by Li et al.[238] and Xie et al.[239] respectively. Type-I Weyl points were observed in chiral phononic crystal and Weyl points with opposite topological charges were distributed in different planes in Brillouin zone. In the constant frequency plane, a pair of chiral Weyl points projected as a point connected by a Fermi arc, as shown in Fig. 7(d)[238]. Type-I Weyl point shows vertical conical dispersion, while the cone dispersion at type-II Weyl point is seriously inclined. When the anisotropic coupling is introduced, the cone dispersion of type-I Weyl point is inclined seriously to become type-II Weyl point. Due to the inclined conical dispersion, the Fermi arc is not a connection between point and point like type-I Weyl point, but a connection between bulk band and bulk band on the constant frequency plane, as shown in Fig. 7(e)[239]. In addition, other novel fermions, such as the triple-degeneracy fermions[240], have been observed successively. More recently, by gapping out the edge states, higher-order topological insulators, which host both topological corner and hinge states, got a lot of attention[241–245]. Zhang et al. observed the topologically protected corner and hinge states at the interface of two 2D photonic crystal carrying Dirac mass of unequal size and opposite sign[241]. Based on the theory of charge polarization, it is found that a 2D quantized quadrupole insulator has similar topological one-dimensional edge modes with gaps, which stabilize zero dimensional in-gap corner states[246–248]. The corresponding tight bound model with alternating distribution of positive and negative coupling is shown in Fig. 7(f)[248]. The quantized quadrupole is concentrated at the four corners of the unit cell and the corner states exist in the four corners of the sample shown in Fig. 7(f).

Applications in wave field manipulations

Applications in EM manipulations

Based on the outstanding EM wave manipulation abilities of metasurfaces, numerous useful applications have been proposed. In this section, we will introduce some important applications of metasurfaces, including structural colors, polarization measurements, optical sensors and optical information encryptions.

Structural colors exist widely in nature and human society, which originate from the interference between incident light and microstructures[249–251]. Structures with different shapes and geometrical parameters can display various colors due to their different resonant properties in the visible region. Structural colors based on metasurfaces have many advantages compared with chemical pigments, such as high spatial resolution, high durability, low pollution and being tunable by structural change. Over the past decades, plenty of structural colors have been realized and studied by using plasmonic structures, both in reflective[252–254] and transmissive[255–257] schemes. However, plasmonic structures often have the disadvantages of high losses, broad peak widths and prohibitive costs, which hinder their practical uses in realizing high purity structural colors. One method to tackle this problem is to use the dielectric structures[258–264]. Recently, a metasurface based on multi-dielectric stacked layer structures has been proposed to realize ultrahigh saturation structural colors[265]. As shown in Fig. 8(a), the unit cell consists of three dielectric layers, which can realize the deep modulation of multipolar modes. By suppressing the multipolar modes at higher frequencies, the saturation and gamut space of structural colors can be dramatically increased. The measured saturation can reach about 90% and the simulated gamut space can occupy 171% sRGB space, 127% Adobe RGB space and 90% Recommendation 2020 space. The huge gamut space and ultrahigh saturation of structural colors indicates that the metasurface-based structural colors have enormous potentials in advanced color display devices. However, there are still some obstacles needed to be addressed on the road to practical applications of structural colors, such as mass production, dynamic color display and high-quality additive colors in the transmission mode.

Polarization measurement plays a vital role in polarization communication, remote sensing and spectropolarimetry. However, traditional methods for measuring the states of polarizations (SOPs) often rely on
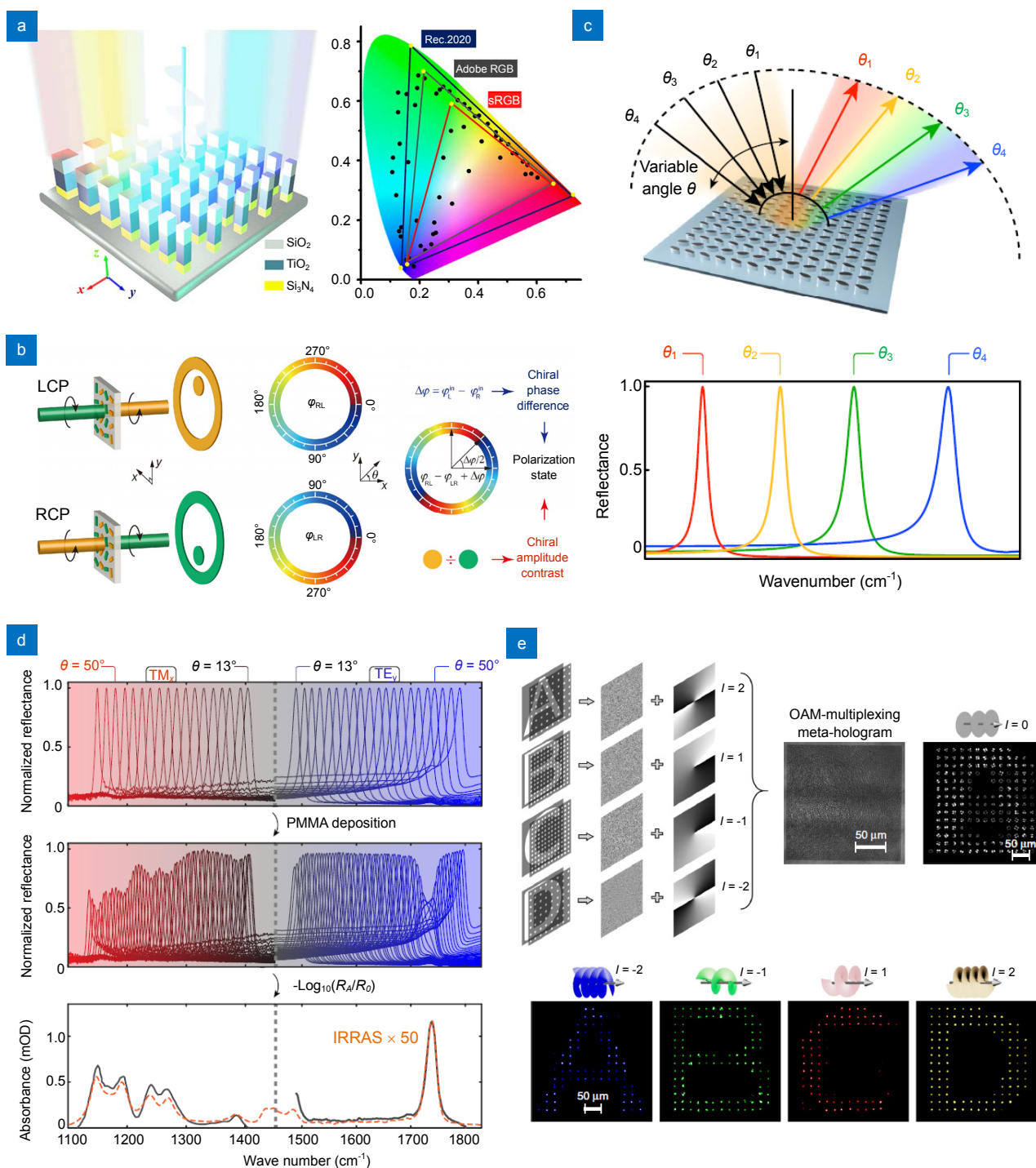
Fig. 8 | (a) Left panel: schematic of the metasurface based on multi-dielectric stacked layer structures that can realize ultrahigh saturation structural colors. Right panel: the simulated CIE 1931 chromaticity coordinates for the samples with different periods and gaps. **(b)** Schematic of the multiplexed hologram metasurface that can realize direct polarization measurement. **(c)** Schematic of the angle-multiplexed all-dielectric metasurface (upper) and the reflection spectra of the metasurface for different incident angles (lower). **(d)** Normalized reflection spectra of the metasurface before (upper) and after (middle) coating a polymethyl methacrylate (PMMA) layer. Lower panel: absorption spectrum obtained from the measured reflection spectra (black line) and absorption spectrum of a PMMA layer on a gold surface obtained from standard infrared reflection absorption spectroscopy measurement (orange dashed line). **(e)** Design approach (upper left) anld experimental characterization (upper right and lower panels) of an OAM-multiplexing hologram metasurface that can encode different holographic images into different OAM channels. Figure reproduced from: (a) ref.[265], American Chemical Society; (b) ref.[284], Optical Society of America; (c–d) ref.[304], American Association for the Advancement of Science.; (e) ref.[313], Nature Publishing Group.

bulky optical components, such as polarizers and waveplates. Metasurfaces can distinguish different polarizations by using subwavelength anisotropic nanostructures[266,267], and thus can be utilized to realize ultracompact polarimeters. Based on photonic spin Hall effect[268–274] or CD effect[275], different CP light can be distinguished and detected. Because a completely polarized light can be decomposed into two CP light with opposite handedness, the ellipticity and handedness of a polarized light can hence be obtained by measuring the intensity ratio of its RCP and LCP components[276]. To fully characterize the SOPs of light, one method is to obtain the full Stokes parameters of light by decomposing the incident light into several pairs of orthogonal polarized light[277–281]. In addition, taking advantage of the intrinsic dispersive behavior of nanostructures, spectropolarimeters that can analyze the SOPs and spectral components of incident light simultaneously have also been realized[90,282–283]. Another method that can measure the SOPs of light is to obtain the amplitudes and phase difference of two orthogonally polarized components simultaneously. Recently, Zhang et al. proposed a multiplexed hologram metasurface that can realize direct polarization measurement[284]. As shown in Fig. 8(b), the metasurface can generate two holographic images of a ring containing an upper circular disk or a lower circular disk for LCP or RCP incident light, respectively. The two ring images can overlap with each other with different PB phase distributions and generate different interference patterns according to the phase difference between LCP and RCP light. In addition, the amplitude contrast of the two CP light can be obtained by comparing the intensities of the upper and lower circular disks. Thus, the SOPs of incident light can be determined by directly measuring the holographic images. This method provides a new way to measure the phase difference between two orthogonally polarized light, which may bring out more compact polarization measurement devices.

Optical sensors based on metamaterials or metasurfaces are widely used in detecting low concentration molecules[285–291] and small refractive index changes of surrounding mediums[292–296]. Most of these optical sensors are based on the strong resonance and local field enhancement of nanostructures, which can improve the sensitivity of optical responses to the changes of the surroundings. To fully characterize the figure of merit (FOM) of an optical sensor, the quality factor (Q-factor) of the resonance also needs to be considered. A higher sensitivity and a higher Q-factor will result in a higher FOM. Many methods and structures have been proposed to improve the Q-factor of the resonance, such as the methods based on Fano resonances[297,298] or bound states in the continuum (BICs)[299,300]. Recently, a new kind of asymmetric dielectric structure that can realize high Q-factor resonances based on the BICs has been proposed[301,302]. When the asymmetry parameter of such a structure approaches zero, the Q-factor can tend to infinity in theory if the material has no absorption loss. This kind of structure was then quickly applied to realize the molecular detections[303–305]. The molecular absorption fingerprints can be obtained by using an angle-multiplexed all-dielectric metasurface[304]. As shown in Fig. 8(c), the metasurface consists of germanium elliptical resonators with asymmetrically tilted main ellipse axes. When a broadband light source illuminates the metasurface at different incident angles, the peak positions of the reflection spectra can change over a target fingerprint range. Taking advantages of the high Q-factor and surface-sensitive resonance, the reflection spectra can be modulated by the absorption of the analyte, as shown in Fig. 8(d). As a result, the distinct absorption fingerprints of different analytes can be obtained by comparing the reflection envelopes before and after analyte coating. These optical sensors based on metasurfaces pave the way for compact and portable diagnostic applications. On the other hand, various optical sensors that can detect different physical quantities, such as depth sensors[306] and quantum sensors[307], can also be realized in the future by using metasurfaces.

Optical information encryption shows its significance in modern society. Using metasurfaces, images can be encoded into different dimensions of EM waves, such as wavelength, polarization and OAM, and thus can only be decoded under specified conditions. For example, Walter et al. encoded the optical images into nonlinear metasurfaces, which can only be read out from SHG waves[308]. In addition, by manipulating the polarization profile of SHG waves, high-resolution images can be encrypted by both the wavelength and polarization simultaneously[309]. There are two major technical proposals for the encryptions based on polarization manipulation. One is encoding the optical information (amplitude or phase) into specified polarization states[310]. The other is using the Malus's law to generate grayscale imags after passing through a linear polarizer[311,312]. Recently, Ren et al. proposed a metasurface that can realize OAM multiplexing

holography, which can encode different holographic images into different OAM channels[313]. To avoid the interference between OAM pixels in the image plane, an OAM-dependent 2D Dirac comb function was used to sample the hologram in the spatial frequency domain. As shown in Fig. 8(e), the OAM multiplexing holography can be realized by superposing four different OAM selective holograms on a single metasurface. If a planar wave with a topological charge of zero incidents on the metasurface, only a complex interference pattern can be observed. However, four different holographic images can be decoded by the incident waves with opposite topological charges to that of the spiral phases used in the encoding processes. This work opens the door of OAM encryption and may greatly increase the capacity of encrypted information. Optical information encryptions can also be realized through controlled chemical reactions. Based on the hydrogenation/dehydrogenation process of magnesium, dynamic information encryptions/decryptions have been realize through metal/dielectric transitions[314,315]. With the help of metasurfaces, more novel methods of optical information encryptions will be proposed in the future.

Besides the abovementioned applications, metasurfaces can also be used in imaging[316-319], invisibility cloak[320-324], photochemistry[325] and some other important research fields. Backlund et al. demonstrated that the orientation-induced lateral localization biases in single-molecule microscopy can be removed by a metasurface-based azimuthal polarization filter placed in the microscope's Fourier plane[316]. Pahlevaninezhad et al. proposed a nano-optical endoscope by integrating a metalens into an endoscopic optical coherence tomography catheter[317]. With the help of metalens, non-chromatic aberrations can be eliminated and high-resolution optical coherence tomography in vivo can be achieved. Based on the phase compensation strategy and the phase manipulation abilities of metasurfaces, Ni et al. experimentally realized an ultrathin invisibility cloak for visible light[320]. However, this invisibility cloak is polarization-sensitive. To realize polarization-insensitive invisibility cloak, Orazbayev et al. proposed a cloak metasurface composed of double coaxial metallic rings[323], which can work for both transverse electric and transverse magnetic incident polarizations. Recently, Chu et al. proposed an invisibility cloak that can operate in transmission geometry by combining transparent metasurfaces and zero-index materials[324]. These applica-

tions based on metasurfaces are expected to innovate in the relevant domains and have potentials in realizing compact and integrated optical devices.

Applications in acoustic manipulations

Because the metasurfaces can flexibly manipulate the amplitude and phase of the acoustic wave, the arbitrary regulation of the sound wave becomes a reality. The transmission, reflection and absorption type metasurfaces with specific phase-amplitude modulation show great application prospects, such as acoustic holography[326,327], acoustic stealth[328], acoustic focusing[329] and sound-absorbing material[330-332]. Melde et al. designed a 3D printed hologram surface that could precisely regulate the phase delay of wavefront, and realized highly resolved acoustic holography[327]. The phase delay of each pixel of the image depends on the thickness of the 3D printed transmission elements. After the sound waves pass through the holographic plane, the sound waves carrying the picture information appear in the image plane, as shown in Fig. 9(a). The hologram modulated by this method has a very high resolution and a pixel accuracy of up to 20 μm , achieving 15,000 acoustic pixels in the hologram. In addition, Xie et al. realized acoustic holography using metasurface active phase arrays as sub-wavelength pixels[326]. A set of 12 optimized labyrinthine unit cells were designed to realize the phase delay profile required by the hologram. By arranging the unit cells, the holographic of a letter 'A' was reconstructed experimentally. The holographic metasurface does not require complicated circuits, but only a sensor, which greatly reduces the complexity of the system and has brought a huge application prospect for the control of acoustic wave and modulation of signal. Yang el at. proposed a single multi-wave metasurface carpet cloak that can hide objects with arbitrary shape and size under EM wave, acoustic wave, and water wave[328]. As shown in Fig. 9(b,c), by providing an additional phase to compensate the phase distortion introduced by a bump, metasurface carpet cloak can strongly suppress the scattering from the bump, thus achieving acoustic stealth. Kaina et al. realized subwavelength focusing only by a metamaterial consisting of a single resonant unit. The Helmholtz resonator structure is introduced into the metamaterial, and the reciprocal of the equivalent mass density and volume modulus of the acoustic metamaterial are all negative by adjusting the size of the structure[333]. Based on the double negative exponential acoustic metamaterial, a negative
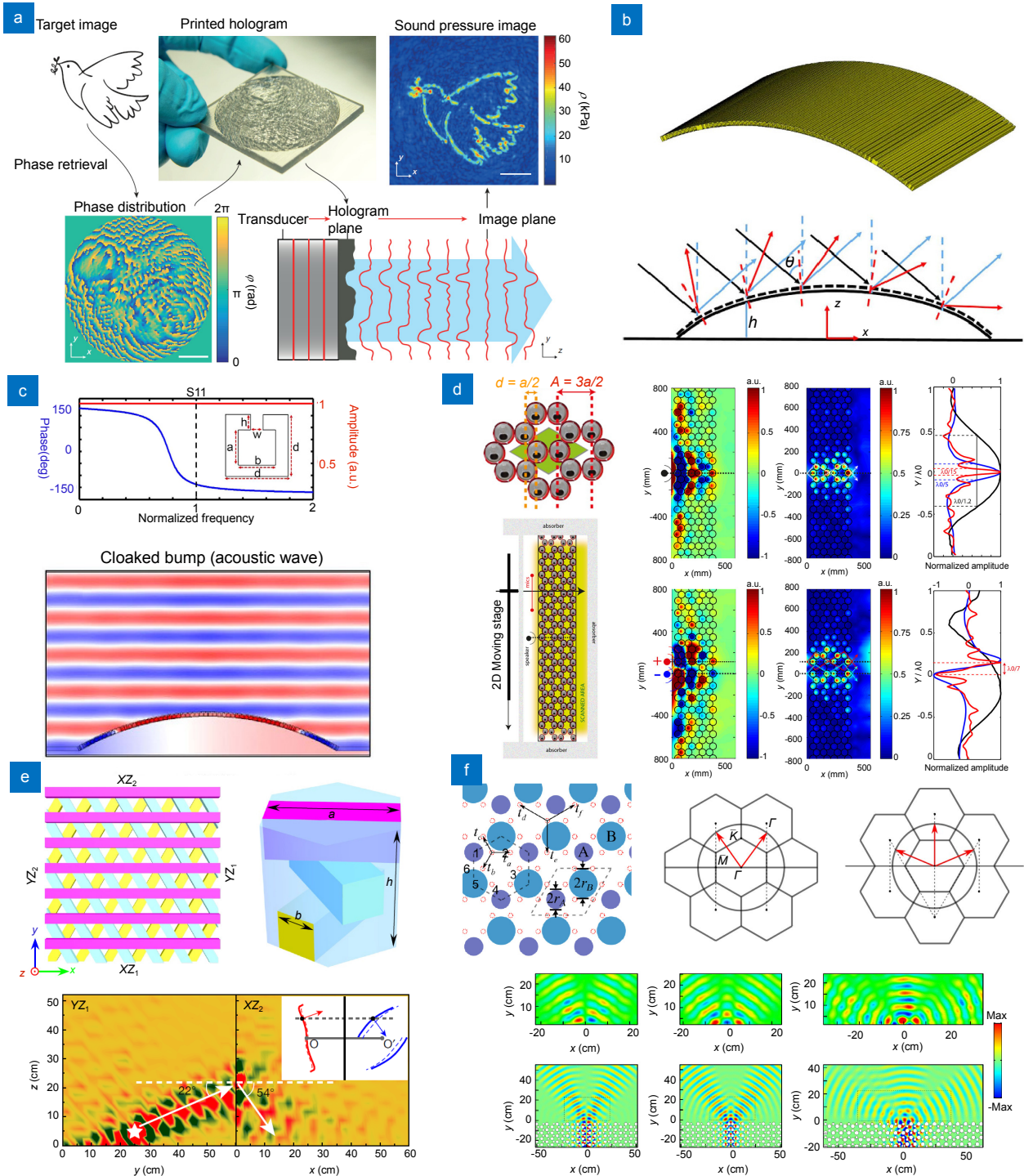
Fig. 9 | (**a**) Schematic of the process of acoustic hologram imaging. Left panels: target image and phase distribution of target image. Middle panel: the metamaterial corresponding to the phase distribution. Right panels: workflow for acoustic metamaterial reconstructing target acoustic images. (**b**) Scheme of a metasurface carpet cloak. The black arrows are the incident waves; the blue arrows and red arrows are the reflected waves with and without metasurface carpet cloak. (**c**) A typical unit cell of the metasurface carpet cloak and its corresponding S11 parameters. (**d**) Left panels: Schematic of the unit cell of flat acoustic superlens and the flat acoustic superlens. Reft panels: experimental demonstration of subwavelength focusing (upper) and imaging (lower) using a flat acoustic superlens. (**e**) Upper panels: schematic of the Weyl phononic crystal and its unit cell. Lower panel: the experimental observation of topological negative refraction. (**f**) Upper panels: schematic of the sonic crystal based on Kekulé lattice (left) and the k-space analysis on the outcoupling of armchair termination at f = 5.6 kHz (middle) and zigzag terminations at f = 5.8 kHz (right). Lower panels: the measurements (upper) and simulations (lower) of three types of topological acoustic antennas corresponding to zigzag domain walls and armchair terminations (left and middle), the armchair domain wall and the zigzag termination (right). Figure reproduced from: (a) ref.[327], Nature Publishing Group; (b–c) ref.[328], Nature Publishing Group; (d) ref.[333], Nature Publishing Group; (e) ref.[335], Nature Publishing Group; (f) ref.[336], American Physical Society.

index acoustic superlens was designed and subwavelength focusing was achieved, as shown in Fig. 9(d), which can realize imaging with spot width and resolution 7 and 3.5 times better than the diffraction limit, respectively. In addition, by taking advantage of the coupling of the Fabry-Pérot resonance mode and evanescent wave, Zhu et al. designed a metamaterial with three-dimensional pipeline structure that enables high-frequency information carrying object details to be observed at the image plane, thus achieving acoustic imaging with resolution of $\lambda/50$[334]. Moreover, the phenomenon of negative refraction has been found in phonon crystals very recently, which has opened up a new way of application of topological phonon crystals. It is found that topological negative refraction effect can be observed on the surfaces formed by cutting and splicing from different surfaces of Weyl phonon crystal[335]. For the semi-open Fermi arc, topological negative refraction, with reflection completely suppressed, behaves differently from traditional negative refraction, as shown in Fig. 9(e). Xie et al. proposed topological directional antenna based on a 2D sonic crystal with a Kekulé lattice. By controlling the parity and angular selectivity of the edge states, the out-coupled edge states can generate one beam, two beams in symmetric or antisymmetric fashion, or multibeams, as shown in Fig. 9(f)[336].

Conclusions and outlook

To summarize, we have reviewed recent progresses of wave field manipulations, including EM wave manipulations and acoustic wave manipulations. The multidimensional EM wave manipulations based on metasurfaces produce plenty of novel applications and show great potentials in realizing miniaturized and integrated multifunctional devices. The manipulations of acoustic waves in air and phononic crystals also have great significances in theoretical studies and practical applications. The methods proposed to manipulate wave fields based on artificial microstructures break the limitations of traditional materials and expand the scope of modern optics and acoustics. Based on the current developments in wave manipulations, some promising directions in this field are foreseeable in the future.

1) Arbitrary dimensional manipulation of EM waves. Arbitrarily manipulating the EM wave fields is one of the ultimate pursuits for researchers. Although many methods have been proposed to realize single-dimensional and 2D manipulations of EM waves, simultaneously manipu-

lating three or more dimensions of EM waves is still a challenging work. Based on chiral geometric metasurfaces, the simultaneous manipulations of amplitude, polarization and phase have been realized[337]. Asymmetric transmission and phase manipulation have also been realized simultaneously by using metasurfaces[338,339]. In addition, polarization controlled complex amplitude holograms[340] and polarization controlled color holograms[341,342] have also been proposed. However, these works cannot arbitrarily and independently manipulate more than two dimensions of EM waves, because some of the optical dimensions are usually associated with each other through the geometrical parameters of the microstructures and the degrees of freedom of the geometrical parameter space are usually not enough. To realize arbitrary dimensional manipulation of EM waves, new methods should be proposed to decouple these optical dimensions and more degrees of freedom may need to be searched to find proper structures. Thus, the design processes of these metasurfaces may be complicated and time-consuming. This problem may be partially solved by using some advanced computational methods and artificial intelligence in the design processes[343–347].

2) On-chip optical dimensional manipulation. Besides the manipulations of free space waves, the manipulations of surface waves and waveguide modes also have great significances for their potential applications in integrated optical circuits and on-chip detectors[348–350]. Based on subwavelength structures, the free space propagating waves can be converted into surface plasmon polaritons[351,352], Cherenkov surface plasmon wakes[353], and waveguide modes[354–357]. In addition, on-chip wavelength demultiplexing[358–360], spatial modes conversion[361] and polarization beamsplitter[362] have also been realized by introducing the subwavelength artificial microstructures into optical waveguides. Notably, by integrating phase gradient metasurfaces with optical waveguides, asymmetric optical power transmission[363] and phase-matching-free SHG[364] in waveguides can be realized. The resonance and scattering properties of nanoantennas provide a bridge to link free space waves and guided waves, and provide a tool to control the propagation properties of waveguide modes. More importantly, by integrating subwavelength structures with on-chip architectures, new optical dimensions in the structure plane can be introduced and manipulated. The manipulation of on-chip optical dimensions and the simultaneous manipulation

of free space waves and guided waves will bring out numerous novel integrated photonic devices.

3) Manipulation of elastic phonons. It is well known that in air or water acoustic systems only the longitudinal wave modes exist, while in elastic wave systems there are not only longitudinal wave mode but also transverse wave mode. Acoustic waves in solid elastomers carry time, frequency, amplitude and phase information, which is similar to fluid system. In addition, because elastic wave phonons have shear wave modes not found in fluid sound waves, elastic phonons have more abundant modes, higher frequencies, and higher energy densities, making them less susceptible to the effects of their surroundings[365–367]. Solid-state devices that manipulate elastic phonons are also easier to be miniaturized and integrated into solid-state chips. Elastic phonons have advantages that fluid phonons do not, such as extensible to integrated devices, strong anti-jamming ability and low loss, which make them have the potential to construct new chip components and have great application potential in modern industrial civilization. Recently, phonon thermal diodes[368], elastic metamaterials[366,369], thermal pumping[370] and other novel materials and devices have been predicted and realized by scientists.

References

1. Liu Y M, Zhang X. Metamaterials: a new frontier of science and technology. *Chem Soc Rev* **40**, 2494–2507 (2011).
2. Zheludev N I, Kivshar Y S. From metamaterials to metadevices. *Nat Mater* **11**, 917–924 (2012).
3. Wong Z J, Wang Y, O'Brien K, Rho J, Yin X B et al. Optical and acoustic metamaterials: superlens, negative refractive index and invisibility cloak. *J Opt* **19**, 084007 (2017).
4. Cheng H, Liu Z C, Chen S Q, Tian J G. Emergent functionality and controllability in few-layer metasurfaces. *Adv Mater* **27**, 5410–5421 (2015).
5. Chen H T, Taylor A J, Yu N F. A review of metasurfaces: physics and applications. *Rep Prog Phys* **79**, 076401 (2016).
6. Genevet P, Capasso F, Aieta F, Khorasaninejad M, Devlin R. Recent advances in planar optics: from plasmonic to dielectric metasurfaces. *Optica* **4**, 139–152 (2017).
7. Yu N F, Capasso F. Flat optics with designer metasurfaces. *Nat Mater* **13**, 139–150 (2014).
8. He Q, Sun S L, Xiao S Y, Zhou L. High-efficiency metasurfaces: principles, realizations, and applications. *Adv Opt Mater* **6**, 1800415 (2018).
9. Assouar B, Liang B, Wu Y, Li Y, Cheng J C et al. Acoustic metasurfaces. *Nat Rev Mater* **3**, 460–472 (2018).
10. Shelby R A, Smith D R, Schultz S. Experimental verification of a negative index of refraction. *Science* **292**, 77–79 (2001).
11. Schurig D, Mock J J, Justice B J, Cummer S A, Pendry J B et al. Metamaterial electromagnetic cloak at microwave frequencies. *Science* **314**, 977–980 (2006).
12. Moitra P, Yang Y M, Anderson Z, Kravchenko I I, Briggs D P et al. Realization of an all-dielectric zero-index optical metamaterial. *Nat Photonics* **7**, 791–795 (2013).
13. Li Y, Kita S, Muñoz P, Reshef O, Vulis D I et al. On-chip zero-index metamaterials. *Nat Photonics* **9**, 738–742 (2015).
14. Sun J B, Litchinitser N M. Toward practical, subwavelength, visible-light photolithography with hyperlens. *ACS Nano* **12**, 542–548 (2018).
15. Kapitanova P V, Ginzburg P, Rodríguez-Fortuño F J, Filonov D S, Voroshilov P M et al. Photonic spin Hall effect in hyperbolic metamaterials for polarization-controlled routing of subwavelength modes. *Nat Commun* **5**, 3226 (2014).
16. Poddubny A, Iorsh I, Belov P, Kivshar Y. Hyperbolic metamaterials. *Nat Photonics* **7**, 948–957 (2013).
17. Lu L, Joannopoulos J D, Soljačić M. Topological photonics. *Nat Photonics* **8**, 821–829 (2014).
18. Wu Y, Li C, Hu X Y, Ao Y T, Zhao Y F et al. Applications of topological photonics in integrated photonic devices. *Adv Opt Mater* **5**, 1700357 (2017).
19. Khanikaev A B, Shvets G. Two-dimensional topological photonics. *Nat Photonics* **11**, 763–773 (2017).
20. Ozawa T, Price H M, Amo A, Goldman N, Hafezi M et al. Topological photonics. *Rev Mod Phys* **91**, 015006 (2019).
21. Ma G C, Xiao M, Chan C T. Topological phases in acoustic and mechanical systems. *Nat Rev Phys* **1**, 281–294 (2019).
22. Cheng H, Chen S Q, Yang H F, Li J J, An X et al. A polarization insensitive and wide-angle dual-band nearly perfect absorber in the infrared regime. *J Opt* **14**, 085102 (2012).
23. Li J X, Yu P, Tang C C, Cheng H, Li J J et al. Bidirectional perfect absorber using free substrate plasmonic metasurfaces. *Adv Opt Mater* **5**, 1700152 (2017).
24. Li Z C, Liu W W, Tang C C, Cheng H, Li Z et al. A bilayer plasmonic metasurface for polarization-insensitive bidirectional perfect absorption. *Adv Theory Simul* **3**, 1900216 (2020).
25. Fang Z Y, Cai J Y, Yan Z B, Nordlander P, Halas N J et al. Removing a wedge from a metallic nanodisk reveals a Fano resonance. *Nano Lett* **11**, 4475–4479 (2011).
26. Duan X Y, Chen S Q, Yang H F, Cheng H, Li J J et al. Polarization-insensitive and wide-angle plasmonically induced transparency by planar metamaterials. *Appl Phys Lett* **101**, 143105 (2012).
27. Chen H T, Zhou J F, O'Hara J F, Chen F, Azad A K et al. Antireflection coating using metamaterials and identification of its mechanism. *Phys Rev Lett* **105**, 073901 (2010).
28. Huang L, Chang C C, Zeng B B, Nogan J, Luo S N et al. Bilayer metasurfaces for dual- and broadband optical antireflection. *ACS Photonics* **4**, 2111–2116 (2017).
29. Gansel J K, Thiel M, Rill M S, Decker M, Bade K et al. Gold helix photonic metamaterial as broadband circular polarizer. *Science* **325**, 1513–1515 (2009).
30. Zhao Y, Alù A. Tailoring the dispersion of plasmonic nanorods to realize broadband optical meta-waveplates. *Nano Lett* **13**, 1086–1091 (2013).
31. Wan W W, Gao J, Yang X D. Metasurface holograms for holographic imaging. *Adv Opt Mater* **5**, 1700541 (2017).
32. Ding F, Pors A, Bozhevolnyi S I. Gradient metasurfaces: a review of fundamentals and applications. *Rep Prog Phys* **81**, 026401 (2018).
33. Akram M R, Ding G, Chen K, Feng Y, Zhu W. Ultrathin Single Layer Metasurfaces with Ultra-Wideband Operation for Both Transmission and Reflection. *Adv Mater* **32**, 1907308 (2020).
34. Huang L L, Chen X Z, Mühlenbernd H, Li G X, Bai B F et al.

Dispersionless phase discontinuities for controlling light propagation. *Nano Lett* **12**, 5750–5755 (2012).

35. Khorasaninejad M, Capasso F. Metalenses: Versatile multifunctional photonic components. *Science* **358**, eaam8100 (2017).

36. Liu S, Cui T J. Concepts, working principles, and applications of coding and programmable metamaterials. *Adv Opt Mater* **5**, 1700624 (2017).

37. Li G X, Zhang S, Zentgraf T. Nonlinear photonic metasurfaces. *Nat Rev Mater* **2**, 17010 (2017).

38. Chen S Q, Li Z, Zhang Y B, Cheng H, Tian J G. Phase manipulation of electromagnetic waves with metasurfaces and its applications in nanophotonics. *Adv Opt Mater* **6**, 1800104 (2018).

39. Wen D D, Yue F Y, Liu W W, Chen S Q, Chen X Z. Geometric metasurfaces for ultrathin optical devices. *Adv Opt Mater* **6**, 1800348 (2018).

40. Glybovski S B, Tretyakov S A, Belov P A, Kivshar Y S, Simovski C R. Metasurfaces: From microwaves to visible. *Phys Rep* **634**, 1–72 (2016).

41. Sun S L, He Q, Hao J M, Xiao S Y, Zhou L. Electromagnetic metasurfaces: physics and applications. *Adv Opt Photonics* **11**, 380–479 (2019).

42. Chen S Q, Li Z C, Liu W W, Cheng H, Tian J G. From single-dimensional to multidimensional manipulation of optical waves with metasurfaces. *Adv Mater* **31**, 1802458 (2019).

43. Chen S Q, Liu W W, Li Z C, Cheng H, Tian J G. Metasurface-empowered optical multiplexing and multifunction. *Adv Mater* **32**, 1805912 (2020).

44. Chen S Q, Zhang Y B, Li Z, Cheng H, Tian J G. Empowered layer effects and prominent properties in few-layer metasurfaces. *Adv Opt Mater* **7**, 1801477 (2019).

45. Wang Q, Zhang X Q, Xu Y H, Gu J Q, Li Y F et al. Broadband metasurface holograms: toward complete phase and amplitude engineering. *Sci Rep* **6**, 32867 (2016).

46. Ni X J, Kildishev A V, Shalaev V M. Metasurface holograms for visible light. *Nat Commun* **4**, 2807 (2013).

47. Teo J Y H, Wong L J, Molardi C, Genevet P. Controlling electromagnetic fields at boundaries of arbitrary geometries. *Phys Rev A* **94**, 023820 (2016).

48. Ding J, Xu N N, Ren H, Lin Y K, Zhang W L et al. Dual-wavelength terahertz metasurfaces with independent phase and amplitude control at each wavelength. *Sci Rep* **6**, 34020 (2016).

49. Liu Z C, Chen S Q, Li J X, Cheng H, Li Z C et al. Fully interferometric controllable anomalous refraction efficiency using cross modulation with plasmonic metasurfaces. *Opt Lett* **39**, 6763–6766 (2014).

50. Liu Z C, Chen S Q, Cheng H, Li Z C, Liu W W et al. Interferometric control of signal light intensity by anomalous refraction with plasmonic metasurface. *Plasmonics* **11**, 353–358 (2016).

51. Kim M, Wong A M H, Eleftheriades G V. Optical Huygens' metasurfaces with independent control of the magnitude and phase of the local reflection coefficients. *Phys Rev X* **4**, 041042 (2014).

52. Jia S L, Wan X, Su P, Zhao Y J, Cui T J. Broadband metasurface for independent control of reflected amplitude and phase. *AIP Adv* **6**, 045024 (2016).

53. Liu L X, Zhang X Q, Kenney M, Su X Q, Xu N N et al. Broadband metasurfaces with simultaneous control of phase and amplitude. *Adv Mater* **26**, 5031–5036 (2014).

54. Wan X, Jia S L, Cui T J, Zhao Y J. Independent modulations of the transmission amplitudes and phases by using Huygens metasurfaces. *Sci Rep* **6**, 25639 (2016).

55. Song X, Huang L L, Tang C C, Li J J, Li X W et al. Selective diffraction with complex amplitude modulation by dielectric metasurfaces. *Adv Opt Mater* **6**, 1701181 (2018).

56. Arbabi A, Faraon A. Fundamental limits of ultrathin metasurfaces. *Sci Rep* **7**, 43722 (2017).

57. Sun S L, Yang K Y, Wang C M, Juan T K, Chen W T et al. High-efficiency broadband anomalous reflection by gradient meta-surfaces. *Nano Lett* **12**, 6223–6229 (2012).

58. Li Z, Cheng H, Liu Z C, Chen S Q, Tian J G. Plasmonic airy beam generation by both phase and amplitude modulation with metasurfaces. *Adv Opt Mater* **4**, 1230–1235 (2016).

59. Jin J J, Pu M B, Wang Y Q, Li X, Ma X L et al. Multi-channel vortex beam generation by simultaneous amplitude and phase modulation with two-dimensional metamaterial. *Adv Mater Technol* **2**, 1600201 (2017).

60. Lee G Y, Yoon G, Lee S Y, Yun H, Cho J et al. Complete amplitude and phase control of light using broadband holographic metasurfaces. *Nanoscale* **10**, 4237–4245 (2018).

61. Zhou Y, Kravchenko, I I, Wang H, Zheng H Y, Gu G et al. Multifunctional metaoptics based on bilayer metasurfaces. *Light Sci Appl* **8**, 80 (2019).

62. Overvig A C, Shrestha S, Malek S C, Lu M, Stein A et al. Dielectric metasurfaces for complete and independent control of the optical amplitude and phase. *Light Sci Appl* **8**, 92 (2019).

63. Liu W W, Li Z C, Li Z, Cheng H, Tang C C et al. Energy-tailorable spin-selective multifunctional metasurfaces with full Fourier components. *Adv Mater* **31**, 1901729 (2019).

64. Hao W M, Deng M, Chen S Q, Chen L. High-efficiency generation of airy beams with Huygens' metasurface. *Phys Rev Appl* **11**, 054012 (2019).

65. Grady N K, Heyes J E, Chowdhury D R, Zeng Y, Reiten M T et al. Terahertz metamaterials for linear polarization conversion and anomalous refraction. *Science* **340**, 1304–1307 (2013).

66. Yang Y M, Wang W Y, Moitra P, Kravchenko I I, Briggs D P et al. Dielectric meta-reflectarray for broadband linear polarization conversion and optical vortex generation. *Nano Lett* **14**, 1394–1399 (2014).

67. Cong L Q, Xu N N, Gu J Q, Singh R, Han J G et al. Highly flexible broadband terahertz metamaterial quarter-wave plate. *Laser Photonics Rev* **8**, 626–632 (2014).

68. Ding F, Wang Z X, He S L, Shalaev V M, Kildishev A V. Broadband high-efficiency half-wave plate: a supercell-based plasmonic metasurface approach. *ACS Nano* **9**, 4111–4119 (2015).

69. Liu W W, Chen S Q, Li Z C, Cheng H, Yu P et al. Realization of broadband cross-polarization conversion in transmission mode in the terahertz region using a single-layer metasurface. *Opt Lett* **40**, 3185–3188 (2015).

70. Liu Z C, Li Z C, Liu Z, Cheng H, Liu W W et al. Single-layer plasmonic metasurface half-wave plates with wavelength-independent polarization conversion angle. *ACS Photonics* **4**, 2061–2069 (2017).

71. Wu S, Zhang Z, Zhang Y, Zhang K Y, Zhou L et al. Enhanced rotation of the polarization of a light beam transmitted through a silver film with an array of perforated S-shaped holes. *Phys Rev Lett* **110**, 207401 (2013).

72. Fan R H, Zhou Y, Ren X P, Peng R W, Jiang S C et al. Freely tunable broadband polarization rotator for terahertz waves. *Adv Mater* **27**, 1201–1206 (2015).

73. Pfeiffer C, Grbic A. Controlling vector Bessel beams with metasurfaces. *Phys Rev Appl* **2**, 044012 (2014).

74. Yue F Y, Wen D D, Xin J T, Gerardot B D, Li J S et al. Vector vortex beam generation with a single plasmonic metasurface. *ACS Photonics* **3**, 1558–1563 (2016).

75. Zuo R Z, Liu W W, Cheng H, Chen S Q, Tian J G. Breaking the diffraction limit with radially polarized light based on dielectric metalenses. *Adv Opt Mater* **6**, 1800795 (2018).

76. Yu N F, Aieta F, Genevet P, Kats M A, Gaburro Z et al. A broadband, background-free quarter-wave plate based on plasmonic metasurfaces. *Nano Lett* **12**, 6328–6333 (2012).

77. Shaltout A, Liu J J, Shalaev V M, Kildishev A V. Optically active metasurface with non-chiral plasmonic nanoantennas. *Nano Lett* **14**, 4426–4431 (2014).

78. Yu P, Li J X, Tang C C, Cheng H, Liu Z C et al. Controllable optical activity with non-chiral plasmonic metasurfaces. *Light Sci Appl* **5**, e16096 (2016).

79. Wu P C, Tsai W Y, Chen W T, Huang Y W, Chen T Y et al. Versatile polarization generation with an aluminum plasmonic metasurface. *Nano Lett* **17**, 445–452 (2017).

80. Wen D D, Yue F Y, Zhang C M, Zang X F, Liu H G et al. Plasmonic metasurface for optical rotation. *Appl Phys Lett* **111**, 023102 (2017).

81. Ma H F, Liu Y Q, Luan K, Cui T J. Multi-beam reflections with flexible control of polarizations by using anisotropic metasurfaces. *Sci Rep* **6**, 39390 (2016).

82. Li T Y, Huang L L, Liu J, Wang Y T, Zentgraf T. Tunable wave plate based on active plasmonic metasurfaces. *Opt Express* **25**, 4216–4226 (2017).

83. Li J X, Chen S Q, Yang H F, Li J J, Yu P et al. Simultaneous control of light polarization and phase distributions using plasmonic metasurfaces. *Adv Funct Mater* **25**, 704–710 (2015).

84. Yu P, Chen S Q, Li J X, Cheng H, Li Z C et al. Generation of vector beams with arbitrary spatial variation of phase and linear polarization using plasmonic metasurfaces. *Opt Lett* **40**, 3229–3232 (2015).

85. Arbabi A, Horie Y, Bagheri M, Faraon A. Dielectric metasurfaces for complete control of phase and polarization with subwavelength spatial resolution and high transmission. *Nat Nanotechnol* **10**, 937–943 (2015).

86. Pfeiffer C, Grbic A. Cascaded metasurfaces for complete phase and polarization control. *Appl Phys Lett* **102**, 231116 (2013).

87. Deng Z L, Deng J H, Zhuang X, Wang S, Li K F et al. Diatomic metasurface for vectorial holography. *Nano Lett* **18**, 2885–2892 (2018).

88. Khorasaninejad M, Ambrosio A, Kanhaiya P, Capasso F. Broadband and chiral binary dielectric meta-holograms. *Sci Adv* **2**, e1501258 (2016).

89. Wen D D, Yue F Y, Li G X, Zheng G X, Chan K et al. Helicity multiplexed broadband metasurface holograms. *Nat Commun* **6**, 8241 (2015).

90. Maguid E, Yulevich I, Veksler D, Kleiner V, Brongersma M L et al. Photonic spin-controlled multifunctional shared-aperture antenna array. *Science* **352**, 1202–1206 (2016).

91. Cai T, Tang S W, Wang G M, Xu H X, Sun S L et al. High-performance bifunctional metasurfaces in transmission and reflection geometries. *Adv Opt Mater* **5**, 1600506 (2017).

92. Yue F Y, Wen D D, Zhang C M, Gerardot B D, Wang W et al. Multichannel polarization-controllable superpositions of orbital angular momentum states. *Adv Mater* **29**, 1603838 (2017).

93. Zhou J X, Qian H L, Hu G W, Luo H L, Wen S C et al. Broadband photonic spin hall meta-lens. *ACS Nano* **12**, 82–88 (2018).

94. Markovich H, Shishkin I I, Hendler N, Ginzburg P. Optical manipulation along an optical axis with a polarization sensitive meta-lens. *Nano Lett* **18**, 5024–5029 (2018).

95. Mueller J P B, Rubin N A, Devlin R C, Groever B, Capasso F. Metasurface polarization optics: independent phase control of arbitrary orthogonal states of polarization. *Phys Rev Lett* **118**, 113901 (2017).

96. Wang D P, Hwang Y, Dai Y M, Si G Y, Wei S B et al. Broadband high-efficiency chiral splitters and holograms from dielectric nanoarc metasurfaces. *Small* **15**, 1900483 (2019).

97. Deng Z L, Deng J H, Zhuang X, Wang S, Shi T et al. Facile metagrating holograms with broadband and extreme angle tolerance. *Light Sci Appl* **7**, 78 (2018).

98. Chen W T, Yang K Y, Wang C M, Huang Y W, Sun G et al. High-efficiency broadband meta-hologram with polarization-controlled dual images. *Nano Lett* **14**, 225–230 (2014).

99. Montelongo Y, Tenorio-Pearl J O, Milne W I, Wilkinson T D. Polarization switchable diffraction based on subwavelength plasmonic nanoantennas. *Nano Lett* **14**, 294–298 (2014).

100. Devlin R C, Ambrosio A, Rubin N A, Mueller J P B, Capasso F. Arbitrary spin–to–orbital angular momentum conversion of light. *Science* **358**, 896–901 (2017).

101. Huang Y W, Rubin N A, Ambrosio A, Shi Z J, Devlin R C et al. Versatile total angular momentum generation using cascaded J-plates. *Opt Express* **27**, 7469–7484 (2019).

102. Karimi E, Schulz S A, De Leon I, Qassim H, Upham J et al. Generating optical orbital angular momentum at visible wavelengths using a plasmonic metasurface. *Light Sci Appl* **3**, e167 (2014).

103. Chen S M, Cai Y, Li G X, Zhang S, Cheah K W. Geometric metasurface fork gratings for vortex-beam generation and manipulation. *Laser Photonics Rev* **10**, 322–326 (2016).

104. Guo Y H, Pu M B, Zhao Z Y, Wang Y Q, Jin J et al. Merging geometric phase and plasmon retardation phase in continuously shaped metasurfaces for arbitrary orbital angular momentum generation. *ACS Photonics* **3**, 2022–2029 (2016).

105. Zhao H, Quan B G, Wang X K, Gu C Z, Li J J et al. Demonstration of orbital angular momentum multiplexing and demultiplexing based on a metasurface in the Terahertz Band. *ACS Photonics* **5**, 1726–1732 (2018).

106. Veksler D, Maguid E, Shitrit N, Ozeri D, Kleiner V et al. Multiple wavefront shaping by metasurface based on mixed random antenna groups. *ACS Photonics* **2**, 661–667 (2015).

107. Zeng J W, Li L, Yang X D, Gao J. Generating and separating twisted light by gradient-rotation split-ring antenna metasurfaces. *Nano Lett* **16**, 3101–3108 (2016).

108. Li Y, Li X, Chen L W, Pu M B, Jin J J et al. Orbital angular momentum multiplexing and demultiplexing by a single metasurface. *Adv Opt Mater* **5**, 1600502 (2017).

109. Wang S, Li F J, Deng J H, Ye X, Deng Z L et al. Diatomic metasurface based broadband J-plate for arbitrary spin-to-orbital conversion. *J Phys D: Appl Phys* **52**, 324002 (2019).

110. Menzel C, Helgert C, Rockstuhl C, Kley E B, Tunnermann A et al. Asymmetric transmission of linearly polarized light at optical metamaterials. *Phys Rev Lett* **104**, 253902 (2010).

111. Huang C, Feng Y J, Zhao J M, Wang Z B, Jiang T. Asymmetric electromagnetic wave transmission of linear polarization via polarization conversion through chiral metamaterial structures. *Phys Rev B* **85**, 195131 (2012).

112. Kenanakis G, Xomalis A, Selimis A, Vamvakaki M, Farsari M et

al. Three-dimensional infrared metamaterial with asymmetric transmission. *ACS Photonics* **2**, 287–294 (2015).

113. Mutlu M, Akosman A E, Serebryannikov A E, Ozbay E. Diodelike asymmetric transmission of linearly polarized waves using magnetoelectric coupling and electromagnetic wave tunneling. *Phys Rev Lett* **108**, 213905 (2012).

114. Pfeiffer C, Zhang C, Ray V, Guo L J, Grbic A. High performance bianisotropic metasurfaces: asymmetric transmission of light. *Phys Rev Lett* **113**, 023902 (2014).

115. Zhang C, Pfeiffer C, Jang T, Ray V, Junda M et al. Breaking Malus' law: Highly efficient, broadband, and angular robust asymmetric light transmitting metasurface. *Laser Photonics Rev* **10**, 791–798 (2016).

116. Li Z C, Chen S Q, Tang C C, Liu W W, Cheng H et al. Broadband diodelike asymmetric transmission of linearly polarized light in ultrathin hybrid metamaterial. *Appl Phys Lett* **105**, 201103 (2014).

117. Li Z C, Chen S Q, Liu W W, Cheng H, Liu Z C et al. High performance broadband asymmetric polarization conversion due to polarization-dependent reflection. *Plasmonics* **10**, 1703–1711 (2015).

118. Ji R N, Wang S W, Liu X X, Chen X S, Lu W. Broadband circular polarizers constructed using helix-like chiral metamaterials. *Nanoscale* **8**, 14725–14729 (2016).

119. Zhao Y, Shi J W, Sun L Y, Li X Q, Alù A. Alignment-free three-dimensional optical metamaterials. *Adv Mater* **26**, 1439–1445 (2014).

120. Karimullah A S, Jack C, Tullius R, Rotello V M, Cooke G et al. Disposable plasmonics: plastic templated plasmonic metamaterials with tunable chirality. *Adv Mater* **27**, 5610–5616 (2015).

121. Khanikaev A B, Arju N, Fan Z, Purtseladze D, Lu F et al. Experimental demonstration of the microscopic origin of circular dichroism in two-dimensional metamaterials. *Nat Commun* **7**, 12045 (2016).

122. Rodrigues S P, Lan S F, Kang L, Cui Y H, Panuski P W et al. Intensity-dependent modulation of optically active signals in a chiral metamaterial. *Nat Commun* **8**, 14602 (2017).

123. Liu M K, Powell D A, Guo R, Shadrivov I V, Kivshar Y S. Polarization-induced chirality in metamaterials via optomechanical interaction. *Adv Opt Mater* **5**, 1600760 (2017).

124. Yang S Y, Liu Z, Hu S, Jin A Z, Yang H F et al. Spin-selective transmission in chiral folded metasurfaces. *Nano Lett* **19**, 3432–3439 (2019).

125. Zang X F, Dong F L, Yue F Y, Zhang C M, Xu L H et al. Polarization encoded color image embedded in a dielectric metasurface. *Adv Mater* **30**, 1707499 (2018).

126. Li Z C, Liu W W, Cheng H, Choi D Y, Chen S Q et al. Arbitrary manipulation of light intensity by bilayer aluminum metasurfaces. *Adv Opt Mater* **7**, 1900260 (2019).

127. Menzel C, Rockstuhl C, Lederer F. Advanced Jones calculus for the classification of periodic metamaterials. *Phys Rev A* **82**, 053811 (2010).

128. Shi J H, Ma H F, Guan C Y, Wang Z P, Cui T J. Broadband chirality and asymmetric transmission in ultrathin 90°-twisted Babinet-inverted metasurfaces. *Phys Rev B* **89**, 165128 (2014).

129. Parappurath N, Alpeggiani F, Kuipers L, Verhagen E. The origin and limit of asymmetric transmission in chiral resonators. *ACS Photonics* **4**, 884–890 (2017).

130. Pfeiffer C, Grbic A. Bianisotropic metasurfaces for optimal polarization control: analysis and synthesis. *Phys Rev Appl* **2**, 044011 (2014).

131. Li Z F, Mutlu M, Ozbay E. Chiral metamaterials: from optical activity and negative refractive index to asymmetric transmission. *J Opt* **15**, 023001 (2013).

132. Wang Z J, Cheng F, Winsor T, Liu Y M. Optical chiral metamaterials: a review of the fundamentals, fabrication methods and applications. *Nanotechnology* **27**, 412001 (2016).

133. Qiu M, Zhang L, Tang Z X, Jin W, Qiu C W et al. 3D metaphotonic nanostructures with intrinsic chirality. *Adv Funct Mater* **28**, 1803147 (2018).

134. Bochenkov V E, Shabatina T I. Chiral plasmonic biosensors. *Biosensors* **8**, 120 (2018).

135. Helgert C, Pshenay-Severin E, Falkner M, Menzel C, Rockstuhl C et al. Chiral metamaterial composed of three-dimensional plasmonic nanostructures. *Nano Lett* **11**, 4400–4404 (2011).

136. Hentschel M, Schäferling M, Metzger B, Giessen H. Plasmonic diastereomers: adding up chiral centers. *Nano Lett* **13**, 600–606 (2013).

137. Yin X H, Schäferling M, Metzger B, Giessen H. Interpreting chiral nanophotonic spectra: the plasmonic Born-Kuhn model. *Nano Lett* **13**, 6238–6243 (2013).

138. Hentschel M, Ferry V E, Alivisatos A P. Optical rotation reversal in the optical response of chiral plasmonic nanosystems: the role of plasmon hybridization. *ACS Photonics* **2**, 1253–1259 (2015).

139. Wang Z J, Jia H, Yao K, Cai W S, Chen H S et al. Circular dichroism metamirrors with near-perfect extinction. *ACS Photonics* **3**, 2096–2101 (2016).

140. Hentschel M, Wu L, Schäferling M, Bai P, Li E P et al. Optical properties of chiral three-dimensional plasmonic oligomers at the onset of charge-transfer plasmons. *ACS Nano* **6**, 10355–10365 (2012).

141. Kenney M, Li S X, Zhang X Q, Su X Q, Kim T T et al. Pancharatnam-berry phase induced spin-selective transmission in herringbone dielectric metamaterials. *Adv Mater* **28**, 9567–9572 (2016).

142. Wu C, Arju N, Kelp G, Fan J A, Dominguez J et al. Spectrally selective chiral silicon metasurfaces based on infrared Fano resonances. *Nat Commun* **5**, 3892 (2014).

143. Ye W M, Yuan X D, Guo C C, Zhang J F, Yang B et al. Large chiroptical effects in planar chiral metamaterials. *Phys Rev Appl* **7**, 054003 (2017).

144. Zhou J F, Chowdhury D R, Zhao R K, Azad A K, Chen H T et al. Terahertz chiral metamaterials with giant and dynamically tunable optical activity. *Phys Rev B* **86**, 035448 (2012).

145. Rogacheva A V, Fedotov V A, Schwanecke A S, Zheludev N I. Giant gyrotropy due to electromagnetic-field coupling in a bilayered chiral structure. *Phys Rev Lett* **97**, 177401 (2006).

146. Cui Y H, Kang L, Lan S F, Rodrigues S, Cai W S. Giant chiral optical response from a twisted-arc metamaterial. *Nano Lett* **14**, 1021–1025 (2014).

147. Fasold S, Linß S, Kawde T, Falkner M, Decker M et al. Disorder-enabled pure chirality in bilayer plasmonic metasurfaces. *ACS Photonics* **5**, 1773–1778 (2018).

148. Zhu A Y, Chen W T, Zaidi A, Huang Y W, Khorasaninejad M et al. Giant intrinsic chiro-optical activity in planar dielectric nanostructures. *Light Sci Appl* **7**, 17158 (2018).

149. Hopkins B, Poddubny A N, Miroshnichenko A E, Kivshar Y S. Circular dichroism induced by Fano resonances in planar chiral oligomers. *Laser Photonics Rev* **10**, 137–146 (2016).

150. Ma D N, Li Z C, Zhang Y B, Liu W W, Cheng H et al. Giant spin-selective asymmetric transmission in multipolar-modulated

metasurfaces. *Opt Lett* **44**, 3805–3808 (2019).

151. Liu J Y, Li Z C, Liu W W, Cheng H, Chen S Q et al. High-efficiency mutual dual-band asymmetric transmission of circularly polarized waves with few-layer anisotropic metasurfaces. *Adv Opt Mater* **4**, 2028–2034 (2016).

152. Li Z C, Liu W W, Cheng H, Chen S Q, Tian J G. Tunable dual-band asymmetric transmission for circularly polarized waves with graphene planar chiral metasurfaces. *Opt Lett* **41**, 3142–3145 (2016).

153. Chen Y, Gao J, Yang X D. Direction-controlled bifunctional metasurface polarizers. *Laser Photonics Rev* **12**, 1800198 (2018).

154. Chen Y, Yang X D, Gao J. 3D Janus plasmonic helical nanoapertures for polarization-encrypted data storage. *Light Sci Appl* **8**, 45 (2019).

155. Zhao Y, Belkin M A, Alù A. Twisted optical metamaterials for planarized ultrathin broadband circular polarizers. *Nat Commun* **3**, 870 (2012).

156. Zhao Y, Askarpour A N, Sun L Y, Shi J W, Li X Q et al. Chirality detection of enantiomers using twisted optical metamaterials. *Nat Commun* **8**, 14180 (2017).

157. Wan W W, Gao J, Yang X D. Full-color plasmonic metasurface holograms. *ACS Nano* **10**, 10671–10680 (2016).

158. Wang B, Dong F L, Li Q T, Yang D, Sun C W et al. Visible-frequency dielectric metasurfaces for multiwavelength achromatic and highly dispersive holograms. *Nano Lett* **16**, 5235–5240 (2016).

159. Hu Y Q, Luo X H, Chen Y Q, Liu Q, Li X et al. 3D-Integrated metasurfaces for full-colour holography. *Light Sci Appl* **8**, 86 (2019).

160. Zhang X H, Pu M B, Guo Y H, Jin J J, Li X et al. Colorful metahologram with independently controlled images in transmission and reflection spaces. *Adv Funct Mater* **29**, 1809145 (2019).

161. Wei Q S, Sain B, Wang Y T, Reineke B, Li X W et al. Simultaneous spectral and spatial modulation for color printing and holography using all-dielectric metasurfaces. *Nano Lett* **19**, 8964–8971 (2019).

162. Khorasaninejad M, Aieta F, Kanhaiya P, Kats M A, Genevet P et al. Achromatic metasurface lens at telecommunication wavelengths. *Nano Lett* **15**, 5358–5362 (2015).

163. Aieta F, Kats M A, Genevet P, Capasso F. Multiwavelength achromatic metasurfaces by dispersive phase compensation. *Science* **347**, 1342–1345 (2015).

164. Hu J T, Liu C H, Ren X C, Lauhon L J, Odom T W. Plasmonic lattice lenses for multiwavelength achromatic focusing. *ACS Nano* **10**, 10275–10282 (2016).

165. Arbabi E, Arbabi A, Kamali S M, Horie Y, Faraon A. Multiwavelength polarization-insensitive lenses based on dielectric metasurfaces with meta-molecules. *Optica* **3**, 628–633 (2016).

166. Avayu O, Almeida E, Prior Y, Ellenbogen T. Composite functional metasurfaces for multispectral achromatic optics. *Nat Commun* **8**, 14992 (2017).

167. Yuan G H, Rogers E T, Zheludev N I. Achromatic super-oscillatory lenses with sub-wavelength focusing. *Light Sci Appl* **6**, e17036 (2017).

168. Zhou Y, Kravchenko II, Wang H, Nolen J R, Gu G et al. Multilayer noninteracting dielectric metasurfaces for multiwavelength metaoptics. *Nano Lett* **18**, 7529–7537 (2018).

169. Shi Z J, Khorasaninejad M, Huang Y W, Roques-Carmes C, Zhu A Y et al. Single-layer metasurface with controllable multiwavelength functions. *Nano Lett* **18**, 2420–2427 (2018).

170. Khorasaninejad M, Chen W T, Oh J, Capasso F. Super-dispersive off-axis meta-lenses for compact high resolution spectroscopy. *Nano Lett* **16**, 3732–3737 (2016).

171. Arbabi E, Arbabi A, Kamali S M, Horie Y, Faraon A. Controlling the sign of chromatic dispersion in diffractive optics with dielectric metasurfaces. *Optica* **4**, 625–632 (2017).

172. Li G X, Chen S M, Pholchai N, Reineke B, Wong P W et al. Continuous control of the nonlinearity phase for harmonic generations. *Nat Mater* **14**, 607–612 (2015).

173. Wolf O, Campione S, Benz A, Ravikumar A P, Liu S et al. Phased-array sources based on nonlinear metamaterial nanocavities. *Nat Commun* **6**, 7667 (2015).

174. Segal N, Keren-Zur S, Hendler N, Ellenbogen T. Controlling light with metamaterial-based nonlinear photonic crystals. *Nat Photonics* **9**, 180–184 (2015).

175. Almeida E, Shalem G, Prior Y. Subwavelength nonlinear phase control and anomalous phase matching in plasmonic metasurfaces. *Nat Commun* **7**, 10367 (2016).

176. Tymchenko M, Gomez-Diaz J S, Lee J, Nookala N, Belkin M A et al. Advanced control of nonlinear beams with Pancharatnam-Berry metasurfaces. *Phys Rev B* **94**, 214303 (2016).

177. Chen S M, Li G X, Cheah K W, Zentgraf T, Zhang S. Controlling the phase of optical nonlinearity with plasmonic metasurfaces. *Nanophotonics* **7**, 1013–1024 (2018).

178. Chen S M, Li G X, Zeuner F, Wong W H, Pun E Y B et al. Symmetry-selective third-harmonic generation from plasmonic metacrystals. *Phys Rev Lett* **113**, 033901 (2014).

179. Konishi K, Higuchi T, Li J, Larsson J, Ishii S et al. Polarization-controlled circular second-harmonic generation from metal hole arrays with threefold rotational symmetry. *Phys Rev Lett* **112**, 135502 (2014).

180. Schlickriede C, Waterman N, Reineke B, Georgi P, Li G X et al. Imaging through nonlinear metalens using second harmonic generation. *Adv Mater* **30**, 1703843 (2018).

181. Bar-David J, Levy U. Nonlinear diffraction in asymmetric dielectric metasurfaces. *Nano Lett* **19**, 1044–1051 (2019).

182. Li G X, Sartorello G, Chen S M, Nicholls L H, Li K F et al. Spin and geometric phase control four-wave mixing from metasurfaces. *Laser Photonics Rev* **12**, 1800034 (2018).

183. Almeida E, Bitton O, Prior Y. Nonlinear metamaterials for holography. *Nat Commun* **7**, 12533 (2016).

184. Ye W M, Zeuner F, Li X, Reineke B, He S et al. Spin and wavelength multiplexed nonlinear metasurface holography. *Nat Commun* **7**, 11930 (2016).

185. Li G X, Wu L, Li K F, Chen S M, Schlickriede C et al. Nonlinear metasurface for simultaneous control of spin and orbital angular momentum in second harmonic generation. *Nano Lett* **17**, 7974–7979 (2017).

186. Li Z, Liu W W, Li Z C, Tang C C, Cheng H et al. Tripling the capacity of optical vortices by nonlinear metasurface. *Laser Photonics Rev* **12**, 1800164 (2018).

187. Ma M L, Li Z, Liu W W, Tang C C, Li Z C et al. Optical information multiplexing with nonlinear coding metasurfaces. *Laser Photonics Rev* **13**, 1900045 (2019).

188. Nookala N, Lee J, Tymchenko M, Sebastian Gomez-Diaz J, Demmerle F et al. Ultrathin gradient nonlinear metasurface with a giant nonlinear response. *Optica* **3**, 283–288 (2016).

189. Georgi P, Schlickriede C, Li G X, Zhang S, Zentgraf T. Rotational

Doppler shift induced by spin-orbit coupling of light at spinning metasurfaces. *Optica* **4**, 1000–1005 (2017).

190. Li G X, Zentgraf T, Zhang S. Rotational Doppler effect in nonlinear optics. *Nat Phys* **12**, 736–740 (2016).

191. Czaplicki R, Husu H, Siikanen R, Mäkitalo J, Kauranen M et al. Enhancement of second-harmonic generation from metal nanoparticles by passive elements. *Phys Rev Lett* **110**, 093902 (2013).

192. Lee J, Tymchenko M, Argyropoulos C, Chen P Y, Lu F et al. Giant nonlinear response from plasmonic metasurfaces coupled to intersubband transitions. *Nature* **511**, 65–69 (2014).

193. Celebrano M, Wu X F, Baselli M, Großmann S, Biagioni P et al. Mode matching in multiresonant plasmonic nanoantennas for enhanced second harmonic generation. *Nat Nanotechnol* **10**, 412–417 (2015).

194. Li Z, Liu W W, Li Z C, Cheng H, Chen S Q et al. Fano-resonance-based mode-matching hybrid metasurface for enhanced second-harmonic generation. *Opt Lett* **42**, 3117–3120 (2017).

195. Liu S, Sinclair M B, Saravi S, Keeler G A, Yang Y M et al. Resonantly enhanced second-harmonic generation using III–V semiconductor all-dielectric metasurfaces. *Nano Lett* **16**, 5426–5432 (2016).

196. Yang Y M, Wang W Y, Boulesbaa A, Kravchenko II, Briggs D P et al. Nonlinear fano-resonant dielectric metasurfaces. *Nano Lett* **15**, 7388–7393 (2015).

197. Chen S M, Rahmani M, Li K F, Miroshnichenko A, Zentgraf T et al. Third harmonic generation enhanced by multipolar interference in complementary silicon metasurfaces. *ACS Photonics* **5**, 1671–1675 (2018).

198. Koshelev K, Tang Y T, Li K F, Choi D Y, Li G X et al. Nonlinear metasurfaces governed by bound states in the continuum. *ACS Photonics* **6**, 1639–1644 (2019).

199. Chen S M, Reineke B, Li G X, Zentgraf T, Zhang S. Strong nonlinear optical activity induced by lattice surface modes on plasmonic metasurface. *Nano Lett* **19**, 6278–6283 (2019).

200. Chen S M, Zeuner F, Weismann M, Reineke B, Li G X et al. Giant nonlinear optical activity of achiral origin in planar metasurfaces with quadratic and cubic nonlinearities. *Adv Mater* **28**, 2992–2999 (2016).

201. Nicholls L H, Rodríguez-Fortuño F J, Nasir M E, Córdova-Castro R M, Olivier N et al. Ultrafast synthesis and switching of light polarization in nonlinear anisotropic metamaterials. *Nat Photonics* **11**, 628–633 (2017).

202. Sartorello G, Olivier N, Zhang J J, Yue W S, Gosztola D J et al. Ultrafast optical modulation of second- and third-harmonic generation from cut-disk-based metasurfaces. *ACS Photonics* **3**, 1517–1522 (2016).

203. Keren-Zur S, Tal M, Fleischer S, Mittleman D M, Ellenbogen T. Generation of spatiotemporally tailored terahertz wavepackets by nonlinear metasurfaces. *Nat Commun* **10**, 1778 (2019).

204. Yang M, Sheng P. Sound absorption structures: from porous media to acoustic metamaterials. *Annu Rev Mater Res* **47**, 83–114 (2017).

205. Ma G C, Yang M, Xiao S W, Yang Z Y, Sheng P. Acoustic metasurface with hybrid resonances. *Nat Mater* **13**, 873–878 (2014).

206. Yang M, Meng C, Fu C X, Li Y, Yang Z Y et al. Subwavelength total acoustic absorption with degenerate resonators. *Appl Phys Lett* **107**, 104104 (2015).

207. Jiménez N, Huang W, Romero-García V, Pagneux V, Groby J P. Ultra-thin metamaterial for perfect and quasi-omnidirectional sound absorption. *Appl Phys Lett* **109**, 121902 (2016).

208. Jiménez N, Romero-García V, Pagneux V, Groby J P. Quasiperfect absorption by subwavelength acoustic panels in transmission using accumulation of resonances due to slow sound. *Phys Rev B* **95**, 014205 (2017).

209. Jiang X, Liang B, Li R Q, Zou X Y, Yin L L et al. Ultra-broadband absorption by acoustic metamaterials. *Appl Phys Lett* **105**, 243505 (2014).

210. Yang M, Chen S Y, Fu C X, Sheng P. Optimal sound-absorbing structures. *Mater Horiz* **4**, 673–680 (2017).

211. Cummer S A, Christensen J, Alù A. Controlling sound with acoustic metamaterials. *Nat Rev Mater* **1**, 16001 (2016).

212. Cui T J, Qi M Q, Wan X, Zhao J, Cheng Q. Coding metamaterials, digital metamaterials and programmable metamaterials. *Light Sci Appl* **3**, e218 (2014).

213. Xie B Y, Tang K, Cheng H, Liu Z Y, Chen S Q et al. Coding acoustic metasurfaces. *Adv Mater* **29**, 1603507 (2017).

214. Yu N F, Genevet P, Kats M A, Aieta F, Tetienne J P et al. Light propagation with phase discontinuities: generalized laws of reflection and refraction. *Science* **334**, 333–337 (2011).

215. Li Y, Liang B, Gu Z M, Zou X Y, Cheng J C. Reflected wavefront manipulation based on ultrathin planar acoustic metasurfaces. *Sci Rep* **3**, 2546 (2013).

216. Xie Y B, Wang W Q, Chen H Y, Konneker A, Popa B I et al. Wavefront modulation and subwavelength diffractive acoustics with an acoustic metasurface. *Nat Commun* **5**, 5553 (2014).

217. Li Y, Jiang X, Li R Q, Liang B, Zou X Y et al. Experimental realization of full control of reflected waves with subwavelength acoustic metasurfaces. *Phys Rev Appl* **2**, 064002 (2014).

218. Zhao J J, Li B W, Chen Z N, Qiu C W. Redirection of sound waves using acoustic metasurface. *Appl Phys Lett* **103**, 151604 (2013).

219. Ding C L, Chen H J, Zhai S L, Liu S, Zhao X P. The anomalous manipulation of acoustic waves based on planar metasurface with split hollow sphere. *J Phys D: Appl Phys* **48**, 045303 (2015).

220. Tang K, Qiu C Y, Ke M Z, Lu J Y, Ye Y T et al. Anomalous refraction of airborne sound through ultrathin metasurfaces. *Sci Rep* **4**, 6517 (2014).

221. Mei J, Wu Y. Controllable transmission and total reflection through an impedance-matched acoustic metasurface. *New J Phys* **16**, 123007 (2014).

222. Xie B Y, Cheng H, Tang K, Liu Z Y, Chen S Q et al. Multiband asymmetric transmission of airborne sound by coded metasurfaces. *Phys Rev Appl* **7**, 024010 (2017).

223. Li Y, Shen C, Xie Y B, Li J F, Wang W Q et al. Tunable asymmetric transmission via lossy acoustic metasurfaces. *Phys Rev Lett* **119**, 035501 (2017).

224. Shi C Z, Dubois M, Wang Y, Zhang X. High-speed acoustic communication by multiplexing orbital angular momentum. *Proc Natl Acad Sci USA* **114**, 7250–7253 (2017).

225. Song K, Kim J, Hur S, Kwak J H, Lee S H et al. Directional reflective surface formed via gradient-impeding acoustic meta-surfaces. *Sci Rep* **6**, 32300 (2016).

226. Zhu Y F, Hu J, Fan X D, Yang J, Liang B et al. Fine manipulation of sound via lossy metamaterials with independent and arbitrary reflection amplitude and phase. *Nat Commun* **9**, 1632 (2018).

227. Tian Y, Wei Q, Cheng Y, Liu X J. Acoustic holography based on composite metasurface with decoupled modulation of phase and amplitude. *Appl Phys Lett* **110**, 191901 (2017).

228. Fleury R, Sounas D L, Sieck C F, Haberman M R, Alù A. Sound

isolation and giant linear nonreciprocity in a compact acoustic circulator. *Science* **343**, 516–519 (2014).

229. Yang Z J, Gao F, Shi X H, Lin X, Gao Z et al. Topological acoustics. *Phys Rev Lett* **114**, 114301 (2015).

230. Ni X, He C, Sun X C, Liu X P, Lu M H et al. Topologically protected one-way edge mode in networks of acoustic resonators with circulating air flow. *New J Phys* **17**, 053016 (2015).

231. Ding Y J, Peng Y G, Zhu Y F, Fan X D, Yang J et al. Experimental demonstration of acoustic chern insulators. *Phys Rev Lett* **122**, 014302 (2019).

232. Wu L H, Hu X. Scheme for achieving a topological photonic crystal by using dielectric material. *Phys Rev Lett* **114**, 223901 (2015).

233. He C, Ni X, Ge H, Sun X C, Chen Y B et al. Acoustic topological insulator and robust one-way sound transport. *Nat Phys* **12**, 1124–1129 (2016).

234. Lu J Y, Qiu C Y, Ye L P, Fan X Y, Ke M Z et al. Observation of topological valley transport of sound in sonic crystals. *Nat Phys* **13**, 369–374 (2017).

235. Lu J Y, Qiu C Y, Ke M Z, Liu Z Y. Valley vortex states in sonic crystals. *Phys Rev Lett* **116**, 093901 (2016).

236. Lu J Y, Qiu C Y, Deng W Y, Huang X Q, Li F et al. Valley topological phases in bilayer sonic crystals. *Phys Rev Lett* **120**, 116802 (2018).

237. Xiao M, Chen W J, He W Y, Chan C T. Synthetic gauge flux and Weyl points in acoustic systems. *Nat Phys* **11**, 920–924 (2015).

238. Li F, Huang X Q, Lu J Y, Ma J H, Liu Z Y. Weyl points and Fermi arcs in a chiral phononic crystal. *Nat Phys* **14**, 30–34 (2018).

239. Xie B Y, Liu H, Cheng H, Liu Z Y, Chen S Q et al. Experimental realization of type-II Weyl points and Fermi arcs in phononic crystal. *Phys Rev Lett* **122**, 104302 (2019).

240. Yang Y H, Sun H X, Xia J P, Xue H R, Gao Z et al. Topological triply degenerate point with double Fermi arcs. *Nat Phys* **15**, 645–649 (2019).

241. Zhang X J, Wang H X, Lin Z K, Tian Y, Xie B Y et al. Second-order topology and multidimensional topological transitions in sonic crystals. *Nat Phys* **15**, 582–588 (2019).

242. Xue H R, Yang Y H, Gao F, Chong Y D, Zhang B L. Acoustic higher-order topological insulator on a kagome lattice. *Nat Mater* **18**, 108–112 (2019).

243. Zhang Z W, Long H Y, Liu C, Shao C, Cheng Y et al. Deep-subwavelength holey acoustic second-order topological insulators. *Adv Mater* **31**, 1904682 (2019).

244. Fan H Y, Xia B Z, Tong L, Zheng S J, Yu D J. Elastic higher-order topological insulator with topologically protected corner states. *Phys Rev Lett* **122**, 204301 (2019).

245. Ezawa M. Higher-order topological insulators and semimetals on the breathing kagome and pyrochlore lattices. *Phys Rev Lett* **120**, 026801 (2018).

246. Benalcazar W A, Bernevig B A, Hughes T L. Quantized electric multipole insulators. *Science* **357**, 61–66(2017).

247. King-Smith R D, Vanderbilt D. Theory of polarization of crystalline solids. *Phys Rev B* **47**, 1651–1654 (1993).

248. Serra-Garcia M, Peri V, Süsstrunk R, Bilal O R, Larsen T et al. Observation of a phononic quadrupole topological insulator. *Nature* **555**, 342–345 (2018).

249. Keshavarz Hedayati M, Elbahri M. Review of metasurface plasmonic structural color. *Plasmonics* **12**, 1463–1479 (2017).

250. Lee T, Jang J, Jeong H, Rho J. Plasmonic- and dielectric-based structural coloring: from fundamentals to practical applications. *Nano Converg* **5**, 1 (2018).

251. Yang B, Cheng H, Chen S Q, Tian J G. Structural colors in metasurfaces: principle, design and applications. *Mater Chem Front* **3**, 750–761 (2019).

252. Tan S J, Zhang L, Zhu D, Goh X M, Wang Y M et al. Plasmonic color palettes for photorealistic printing with aluminum nanostructures. *Nano Lett* **14**, 4023–4029 (2014).

253. Li Z Y, Butun S, Aydin K. Large-area, lithography-free super absorbers and color filters at visible frequencies using ultrathin metallic films. *ACS Photonics* **2**, 183–188 (2015).

254. Kumar K, Duan H G, Hegde R S, Koh S C W, Wei J N et al. Printing colour at the optical diffraction limit. *Nat Nanotechnol* **7**, 557–561 (2012).

255. Li Z B, Clark A W, Cooper J M. Dual color plasmonic pixels create a polarization controlled nano color palette. *ACS Nano* **10**, 492–498 (2016).

256. Heydari E, Sperling J R, Neale S L, Clark A W. Plasmonic color filters as dual-state nanopixels for high-density microimage encoding. *Adv Funct Mater* **27**, 1701866 (2017).

257. Dai P, Wang Y S, Zhu X P, Shi H M, Chen Y Q et al. Transmissive structural color filters using vertically coupled aluminum nanohole/nanodisk array with a triangular-lattice. *Nanotechnology* **29**, 395202 (2018).

258. Sun S, Zhou Z X, Zhang C, Gao Y S, Duan Z H et al. All-dielectric full-color printing with TiO_2 metasurfaces. *ACS Nano* **11**, 4445–4452 (2017).

259. Zhu X L, Yan W, Levy U, Mortensen N A, Kristensen A. Resonant laser printing of structural colors on high-index dielectric metasurfaces. *Sci Adv* **3**, e1602487 (2017).

260. Park C S, Shrestha V R, Yue W J, Gao S, Lee S S et al. Structural color filters enabled by a dielectric metasurface incorporating hydrogenated amorphous silicon nanodisks. *Sci Rep* **7**, 2556 (2017).

261. Nagasaki Y, Suzuki M, Hotta I, Takahara J. Control of Si-based all-dielectric printing color through oxidation. *ACS Photonics* **5**, 1460–1466 (2018).

262. Yang B, Liu W W, Li Z C, Cheng H, Chen S Q et al. Polarization-sensitive structural colors with hue-and-saturation tuning based on all-dielectric nanopixels. *Adv Opt Mater* **6**, 1701009 (2018).

263. Bao Y J, Yu Y, Xu H F, Guo C, Li J T et al. Full-colour nanoprint-hologram synchronous metasurface with arbitrary hue-saturation-brightness control. *Light Sci Appl* **8**, 95 (2019).

264. Lim K T P, Liu H L, Liu Y J, Yang J K W. Holographic colour prints for enhanced optical security by combined phase and amplitude control. *Nat Commun* **10**, 25 (2019).

265. Yang B, Liu W W, Li Z C, Cheng H, Choi D Y et al. Ultrahighly saturated structural colors enhanced by multipolar-modulated metasurfaces. *Nano Lett* **19**, 4221–4228 (2019).

266. Pors A, Nielsen M G, Bernardin T, Weeber J C, Bozhevolnyi S I. Efficient unidirectional polarization-controlled excitation of surface plasmon polaritons. *Light Sci Appl* **3**, e197 (2014).

267. Huang L L, Chen X Z, Bai B F, Tan Q F, Jin G F et al. Helicity dependent directional surface plasmon polariton excitation using a metasurface with interfacial phase discontinuity. *Light Sci Appl* **2**, e70 (2013).

268. Shaltout A, Liu J J, Kildishev A, Shalaev V. Photonic spin Hall effect in gap–plasmon metasurfaces for on-chip chiroptical spectroscopy. *Optica* **2**, 860–863 (2015).

269. Ling X H, Zhou X X, Yi X N, Shu W X, Liu Y C et al. Giant photonic spin Hall effect in momentum space in a structured metamaterial with spatially varying birefringence. *Light Sci Appl*

4, e290 (2015).

270. Li Z C, Liu W W, Cheng H, Chen S Q, Tian J G. Manipulation of the photonic spin hall effect with high efficiency in gold-nanorod-based metasurfaces. *Adv Opt Mater* **5**, 1700413 (2017).

271. Liu Y C, Ke Y G, Luo H L, Wen S C. Photonic spin Hall effect in metasurfaces: a brief review. *Nanophotonics* **6**, 51–70 (2017).

272. Shitrit N, Bretner I, Gorodetski Y, Kleiner V, Hasman E. Optical spin Hall effects in plasmonic chains. *Nano Lett* **11**, 2038–2042 (2011).

273. Luo W J, Xiao S Y, He Q, Sun S L, Zhou L. Photonic spin hall effect with nearly 100% efficiency. *Adv Opt Mater* **3**, 1102–1108 (2015).

274. Luo W J, Sun S L, Xu H X, He Q, Zhou L. Transmissive ultrathin pancharatnam-berry metasurfaces with nearly 100% efficiency. *Phys Rev Appl* **7**, 044033 (2017).

275. Li W, Coppens Z J, Besteiro L V, Wang W Y, Govorov A O et al. Circularly polarized light detection with hot electrons in chiral plasmonic metamaterials. *Nat Commun* **6**, 8379 (2015).

276. Wen D D, Yue F Y, Kumar S, Ma Y, Chen M et al. Metasurface for characterization of the polarization state of light. *Opt Express* **23**, 10272–10281 (2015).

277. Wu P C, Chen J W, Yin C W, Lai Y C, Chung T L et al. Visible metasurfaces for on-chip polarimetry. *ACS Photonics* **5**, 2568–2573 (2018).

278. Pors A, Nielsen M G, Bozhevolnyi S I. Plasmonic metagratings for simultaneous determination of Stokes parameters. *Optica* **2**, 716–723 (2015).

279. Balthasar Mueller J P, Leosson K, Capasso F. Ultracompact metasurface in-line polarimeter. *Optica* **3**, 42–47 (2016).

280. Pors A, Bozhevolnyi S I. Waveguide metacouplers for in-plane polarimetry. *Phys Rev Appl* **5**, 064015 (2016).

281. Lee K, Yun H, Mun S E, Lee G Y, Sung J et al. Ultracompact broadband plasmonic polarimeter. *Laser Photonics Rev* **12**, 1700297 (2018).

282. Chen W T, Török P, Foreman M R, Liao C Y, Tsai W Y et al. Integrated plasmonic metasurfaces for spectropolarimetry. *Nanotechnology* **27**, 224002 (2016).

283. Ding F, Pors A, Chen Y T, Zenin V A, Bozhevolnyi S I. Beam-size-invariant spectropolarimeters using gap-plasmon metasurfaces. *ACS Photonics* **4**, 943–949 (2017).

284. Zhang X Q, Yang S M, Yue W S, Xu Q, Tian C X et al. Direct polarization measurement using a multiplexed Pancharatnam–Berry metahologram. *Optica* **6**, 1190–1198 (2019).

285. Sreekanth K V, Alapan Y, ElKabbash M, Ilker E, Hinczewski M et al. Extreme sensitivity biosensing platform based on hyperbolic metamaterials. *Nat Mater* **15**, 621–627 (2016).

286. Yavas O, Svedendahl M, Dobosz P, Sanz V, Quidant R. On-a-chip biosensing based on all-dielectric nanoresonators. *Nano Lett* **17**, 4421–4426 (2017).

287. Salim A, Lim S. Review of recent metamaterial microfluidic sensors. *Sensors* **18**, 232 (2018).

288. Li Z Y, Zhu Y B, Hao Y F, Gao M, Lu M et al. Hybrid metasurface-based mid-infrared biosensor for simultaneous quantification and identification of monolayer protein. *ACS Photonics* **6**, 501–509 (2019).

289. Liu B W, Chen S, Zhang J C, Yao X, Zhong J H et al. A plasmonic sensor array with ultrahigh figures of merit and resonance linewidths down to 3 nm. *Adv Mater* **30**, 1706031 (2018).

290. Zhu Y B, Li Z Y, Hao Z, DiMarco C, Maturavongsadit P et al. Optical conductivity-based ultrasensitive mid-infrared biosensing on a hybrid metasurface. *Light Sci Appl* **7**, 67 (2018).

291. Sreekanth K V, Sreejith S, Han S, Mishra A, Chen X X et al. Biosensing with the singular phase of an ultrathin metal-dielectric nanophotonic cavity. *Nat Commun* **9**, 369 (2018).

292. Lee Y, Kim S J, Park H, Lee B. Metamaterials and metasurfaces for sensor applications. *Sensors* **17**, 1726 (2017).

293. Gallinet B, Martin O J F. Refractive index sensing with subradiant modes: a framework to reduce losses in plasmonic nanostructures. *ACS Nano* **7**, 6978–6987 (2013).

294. Yang Y M, Kravchenko I I, Briggs D P, Valentine J. All-dielectric metasurface analogue of electromagnetically induced transparency. *Nat Commun* **5**, 5753 (2014).

295. Zhang Y B, Liu W W, Li Z C, Li Z, Cheng H et al. High-quality-factor multiple Fano resonances for refractive index sensing. *Opt Lett* **43**, 1842–1845 (2018).

296. Liu H G, Zheng L, Ma P Z, Zhong Y, Liu B et al. Metasurface generated polarization insensitive Fano resonance for high-performance refractive index sensing. *Opt Express* **27**, 13252–13262 (2019).

297. Luk'yanchuk B, Zheludev N I, Maier S A, Halas N J, Nordlander P et al. The Fano resonance in plasmonic nanostructures and metamaterials. *Nat Mater* **9**, 707–715 (2010).

298. Limonov M F, Rybin M V, Poddubny A N, Kivshar Y S. Fano resonances in photonics. *Nat Photonics* **11**, 543–554 (2017).

299. Hsu C W, Zhen B, Stone A D, Joannopoulos J D, Soljačić M. Bound states in the continuum. *Nat Rev Mater* **1**, 16048 (2016).

300. Koshelev K, Favraud G, Bogdanov A, Kivshar Y, Fratalocchi A. Nonradiating photonics with resonant dielectric nanostructures. *Nanophotonics* **8**, 725–745 (2019).

301. Liu M K, Choi D Y. Extreme Huygens' metasurfaces based on quasi-bound states in the continuum. *Nano Lett* **18**, 8062–8069 (2018).

302. Koshelev K, Lepeshov S, Liu M K, Bogdanov A, Kivshar Y. Asymmetric metasurfaces with high-Q resonances governed by bound states in the continuum. *Phys Rev Lett* **121**, 193903 (2018).

303. Tittl A, Leitis A, Liu M K, Yesilkoy F, Choi D Y et al. Imaging-based molecular barcoding with pixelated dielectric metasurfaces. *Science* **360**, 1105–1109 (2018).

304. Leitis A, Tittl A, Liu M K, Lee B H, Gu M B et al. Angle-multiplexed all-dielectric metasurfaces for broadband molecular fingerprint retrieval. *Sci Adv* **5**, eaaw2871 (2019).

305. Yesilkoy F, Arvelo E R, Jahani Y, Liu M K, Tittl A et al. Ultrasensitive hyperspectral imaging and biodetection enabled by dielectric metasurfaces. *Nat Photonics* **13**, 390–396 (2019).

306. Guo Q, Shi Z J, Huang Y W, Alexander E, Qiu C W et al. Compact single-shot metalens depth sensors inspired by eyes of jumping spiders. *Proc Natl Acad Sci USA* **116**, 22959–22965 (2019).

307. Georgi P, Massaro M, Luo K H, Sain B, Montaut N et al. Metasurface interferometry toward quantum sensors. *Light Sci Appl* **8**, 70 (2019).

308. Walter F, Li G X, Meier C, Zhang S, Zentgraf T. Ultrathin nonlinear metasurface for optical image encoding. *Nano Lett* **17**, 3171–3175 (2017).

309. Tang Y T, Intaravanne Y, Deng J H, Li K F, Chen X Z et al. Nonlinear vectorial metasurface for optical encryption. *Phys Rev Appl* **12**, 024028 (2019).

310. Zhang X H, Pu M B, Jin J J, Li X, Gao P et al. Helicity multiplexed spin-orbit interaction in metasurface for colorized and encrypted

holographic display. *Ann Phys* **529**, 1700248 (2017).

311. Yue F Y, Zhang C M, Zang X F, Wen D D, Gerardot B D et al. High-resolution grayscale image hidden in a laser beam. *Light Sci Appl* **7**, 17129 (2018).

312. Zhang C M, Dong F L, Intaravanne Y, Zang X F, Xu L H et al. Multichannel metasurfaces for anticounterfeiting. *Phys Rev Appl* **12**, 034028 (2019).

313. Ren H R, Briere G, Fang X Y, Ni P N, Sawant R et al. Metasurface orbital angular momentum holography. *Nat Commun* **10**, 2986 (2019).

314. Li J X, Kamin S, Zheng G X, Neubrech F, Zhang S et al. Addressable metasurfaces for dynamic holography and optical information encryption. *Sci Adv* **4**, eaar6768 (2018).

315. Duan X Y, Liu N. Scanning plasmonic color display. *ACS Nano* **12**, 8817–8823 (2018).

316. Backlund M P, Arbabi A, Petrov P N, Arbabi E, Saurabh S et al. Removing orientation-induced localization biases in single-molecule microscopy using a broadband metasurface mask. *Nat Photonics* **10**, 459–462 (2016).

317. Pahlevaninezhad H, Khorasaninejad M, Huang Y W, Shi Z J, Hariri L P et al. Nano-optic endoscope for high-resolution optical coherence tomography in vivo. *Nat Photonics* **12**, 540–547 (2018).

318. Colburn S, Zhan A, Majumdar A. Metasurface optics for full-color computational imaging. *Sci Adv* **4**, eaar2114 (2018).

319. Chen C, Song W G, Chen J W, Wang J H, Chen Y H et al. Spectral tomographic imaging with aplanatic metalens. *Light Sci Appl* **8**, 99 (2019).

320. Ni X J, Wong Z J, Mrejen M, Wang Y, Zhang X. An ultrathin invisibility skin cloak for visible light. *Science* **349**, 1310–1314 (2015).

321. Yang Y H, Jing L Q, Zheng B, Hao R, Yin W Y et al. Full-polarization 3D metasurface cloak with preserved amplitude and phase. *Adv Mater* **28**, 6866–6871 (2016).

322. Zhang J, Mei Z L, Zhang W R, Yang F, Cui T J. An ultrathin directional carpet cloak based on generalized Snell's law. *Appl Phys Lett* **103**, 151115 (2013).

323. Orazbayev B, Mohammadi Estakhri N, Alù A, Beruete M. Experimental demonstration of metasurface-based ultrathin carpet cloaks for millimeter waves. *Adv Opt Mater* **5**, 1600606 (2017).

324. Chu H C, Li Q, Liu B B, Luo J, Sun S L et al. A hybrid invisibility cloak based on integration of transparent metasurfaces and zero-index materials. *Light Sci Appl* **7**, 50 (2018).

325. Wu Y K, Yang W H, Fan Y B, Song Q H, Xiao S M. TiO$_2$ metasurfaces: From visible planar photonics to photochemistry. *Sci Adv* **5**, eaax0939 (2019).

326. Xie Y B, Shen C, Wang W Q, Li J F, Suo D J et al. Acoustic holographic rendering with two-dimensional metamaterial-based passive phased array. *Sci Rep* **6**, 35437 (2016).

327. Melde K, Mark A G, Qiu T, Fischer P. Holograms for acoustics. *Nature* **537**, 518–522 (2016).

328. Yang Y H, Wang H P, Yu F X, Xu Z W, Chen H S. A metasurface carpet cloak for electromagnetic, acoustic and water waves. *Sci Rep* **6**, 20219 (2016).

329. Chen J, Xiao J, Lisevych D, Shakouri A, Fan Z. Deep-subwavelength control of acoustic waves in an ultra-compact metasurface lens. *Nat Commun* **9**, 4920 (2018).

330. Li Y, Assouar B M. Acoustic metasurface-based perfect absorber with deep subwavelength thickness. *Appl Phys Lett* **108**, 063502 (2016).

331. Shen C, Cummer S A. Harnessing multiple internal reflections to

332. design highly absorptive acoustic metasurfaces. *Phys Rev Appl* **9**, 054009 (2018).

332. Merkel A, Theocharis G, Richoux O, Romero-García V, Pagneux V. Control of acoustic absorption in one-dimensional scattering by resonant scatterers. *Appl Phys Lett* **107**, 244102 (2015).

333. Kaina N, Lemoult F, Fink M, Lerosey G. Negative refractive index and acoustic superlens from multiple scattering in single negative metamaterials. *Nature* **525**, 77–81 (2015).

334. Zhu J, Christensen J, Jung J, Martin-Moreno L, Yin X et al. A holey-structured metamaterial for acoustic deep-subwavelength imaging. *Nat Phys* **7**, 52–55 (2011).

335. He H L, Qiu C Y, Ye L P, Cai X X, Fan X Y et al. Topological negative refraction of surface acoustic waves in a Weyl phononic crystal. *Nature* **560**, 61–64 (2018).

336. Xie B Y, Liu H, Cheng H, Liu Z Y, Chen S Q et al. Acoustic topological transport and refraction in a Kekulé Lattice. *Phys Rev Appl* **11**, 044086 (2019).

337. Chen Y, Yang X D, Gao J. Spin-controlled wavefront shaping with plasmonic chiral geometric metasurfaces. *Light Sci Appl* **7**, 84 (2018).

338. Li Z C, Liu W W, Cheng H, Liu J Y, Chen S Q et al. Simultaneous generation of high-efficiency broadband asymmetric anomalous refraction and reflection waves with few-layer anisotropic metasurface. *Sci Rep* **6**, 35485 (2016).

339. Zhang F, Pu M B, Li X, Gao P, Ma X L et al. All-dielectric metasurfaces for simultaneous giant circular asymmetric transmission and wavefront shaping based on asymmetric photonic spin-orbit interactions. *Adv Funct Mater* **27**, 1704295 (2017).

340. Xie Z W, Lei T, Si G Y, Wang X Y, Lin J et al. Meta-holograms with full parameter control of wavefront over a 1000 nm bandwidth. *ACS Photonics* **4**, 2158–2164 (2017).

341. Wang B, Dong F L, Yang D, Song Z W, Xu L H et al. Polarization-controlled color-tunable holograms with dielectric metasurfaces. *Optica* **4**, 1368–1371 (2017).

342. Jin L, Dong Z G, Mei S T, Yu Y F, Wei Z et al. Noninterleaved metasurface for (2^6-1) spin- and wavelength-encoded holograms. *Nano Lett* **18**, 8016–8024 (2018).

343. Ma W, Cheng F, Liu Y M. Deep-learning-enabled on-demand design of chiral metamaterials. *ACS Nano* **12**, 6326–6334 (2018).

344. Liu D J, Tan Y X, Khoram E, Yu Z F. Training deep neural networks for the inverse design of nanophotonic structures. *ACS Photonics* **5**, 1365–1369 (2018).

345. Zhang Q, Liu C, Wan X, Zhang L, Liu S et al. Machine‐learning designs of anisotropic digital coding metasurfaces. *Adv Theory Simul* **2**, 1800132 (2019).

346. Yao K, Unni R, Zheng Y B. Intelligent nanophotonics: merging photonics and artificial intelligence at the nanoscale. *Nanophotonics* **8**, 339–366 (2019).

347. Liu Z W, Yan S, Liu H G, Chen X F. Superhigh-resolution recognition of optical vortex modes assisted by a deep-learning method. *Phys Rev Lett* **123**, 183902 (2019).

348. Cheben P, Halir R, Schmid J H, Atwater H A, Smith D R. Subwavelength integrated photonics. *Nature* **560**, 565–572 (2018).

349. Genevet P, Lin J, Kats M A, Capasso F. Holographic detection of the orbital angular momentum of light with plasmonic photodiodes. *Nat Commun* **3**, 1278 (2012).

350. Sun S L, He Q, Xiao S Y, Xu Q, Li X et al. Gradient-index meta-surfaces as a bridge linking propagating waves and surface waves. *Nat Mater* **11**, 426–431 (2012).

351. Lin J, Mueller J P B, Wang Q, Yuan G H, Antoniou N et al. Polarization-controlled tunable directional coupling of surface plasmon polaritons. *Science* **340**, 331–334 (2013).

352. Sun W J, He Q, Sun S L, Zhou L. High-efficiency surface plasmon meta-couplers: concept and microwave-regime realizations. *Light Sci Appl* **5**, e16003 (2016).

353. Genevet P, Wintz D, Ambrosio A, She A, Blanchard R et al. Controlled steering of Cherenkov surface plasmon wakes with a one-dimensional metamaterial. *Nat Nanotechnol* **10**, 804–809 (2015).

354. Vercruysse D, Neutens P, Lagae L, Verellen N, Van Dorpe P. Single asymmetric plasmonic antenna as a directional coupler to a dielectric waveguide. *ACS Photonics* **4**, 1398–1402 (2017).

355. Bernal Arango F, Kwadrin A, Koenderink A F. Plasmonic antennas hybridized with dielectric waveguides. *ACS Nano* **6**, 10156–10167 (2012).

356. Guo R, Decker M, Setzpfandt F, Gai X, Choi D Y et al. High–bit rate ultra-compact light routing with mode-selective on-chip nanoantennas. *Sci Adv* **3**, e1700007 (2017).

357. Guo Y H, Pu M B, Li X, Ma X L, Song S C et al. Chip-integrated geometric metasurface as a novel platform for directional coupling and polarization sorting by spin–orbit interaction. *IEEE J Sel Top Quantum Electron* **24**, 1–7 (2018).

358. Zhang Y B, Li Z C, Liu W W, Li Z, Cheng H et al. Spin‐selective and wavelength-selective demultiplexing based on waveguide-integrated all-dielectric metasurfaces. *Adv Opt Mater* **7**, 1801273 (2019).

359. Piggott A Y, Lu J, Lagoudakis K G, Petykiewicz J, Babinec T M et al. Inverse design and demonstration of a compact and broadband on-chip wavelength demultiplexer. *Nat Photonics* **9**, 374–377 (2015).

360. Liu Z H, Liu X H, Xiao Z Y, Lu C C, Wang H Q et al. Integrated nanophotonic wavelength router based on an intelligent algorithm. *Optica* **6**, 1367–1373 (2019).

361. Ohana D, Desiatov B, Mazurski N, Levy U. Dielectric metasurface as a platform for spatial mode conversion in nanoscale waveguides. *Nano Lett* **16**, 7956–7961 (2016).

362. Shen B, Wang P, Polson R, Menon R. An integrated-nanophotonics polarization beamsplitter with 2.4 × 2.4 µm^2 footprint. *Nat Photonics* **9**, 378–382 (2015).

363. Li Z Y, Kim M H, Wang C, Han Z H, Shrestha S et al. Controlling propagation and coupling of waveguide modes using phase-gradient metasurfaces. *Nat Nanotechnol* **12**, 675–683 (2017).

364. Wang C, Li Z Y, Kim M H, Xiong X, Ren X F et al. Metasurface-assisted phase-matching-free second harmonic generation in lithium niobate waveguides. *Nat Commun* **8**, 2098 (2017).

365. Li S F, Zhao D G, Niu H, Zhu X F, Zang J F. Observation of elastic topological states in soft materials. *Nat Commun* **9**, 1370 (2018).

366. Mousavi S H, Khanikaev A B, Wang Z. Topologically protected elastic waves in phononic metamaterials. *Nat Commun* **6**, 8682 (2015).

367. Yu S Y, He C, Wang Z, Liu F K, Sun X C et al. Elastic pseudospin transport for integratable topological phononic circuits. *Nat Commun* **9**, 3072 (2018).

368. Li N B, Ren J, Wang L, Zhang G, Hänggi P et al. *Colloquium*: Phononics: Manipulating heat flow with electronic analogs and beyond. *Rev Mod Phys* **84**, 1045–1066 (2012).

369. Guo Y N, Dekorsy T, Hettich M. Topological guiding of elastic waves in phononic metamaterials based on 2D pentamode structures. *Sci Rep* **7**, 18043 (2017).

370. Ren J, Liu S, Li B W. Geometric heat flux for classical thermal transport in interacting open systems. *Phys Rev Lett* **108**, 210603 (2012).

Acknowledgements

Competing interests

The authors declare no competing financial interests.